JLAB USER GROUP

Jefferson Lab PAC 26
Proposal Cover Sheet

This document must be received by close of business Monday,

May 24, 2004 at:

Jefferson Lab
User/International Liaison
Mail Stop 12B
12000 Jefferson Ave
Newport News, VA
23606

Experimental Hall: ___Hall B_________

Days Requested for Approval: ___35___

Proposal Title:

Beyond the Born Approximation: A Precise Comparison of Positron-Proton and Electron-Proton Elastic Scattering in CLAS

Proposal Physics Goals

Indicate any experiments that have physics goals similar to those in your proposal.

Approved, Conditionally Approved, and/or Deferred Experiment(s) or proposals:

E04-019, PR04-020, PR04-008, PR04-009, PR04-014

Contact Person

Name: A. Afanasev, J. Arrington, W. K. Brooks (primary contact), K. Joo, B. A. Raue, L. B. Weinstein

Institution:

Address: 12000 Jefferson Ave., MS 12H

Address: Newport News, VA 23606

City, State, ZIP/ Country:

Phone: 757-269-6391 Fax:

E-Mail: brooksw@jlab.org

Jefferson Lab Use Only

Receipt Date:_______________________________________

By:____

BEAM REQUIREMENTS LIST

JLab Proposal No.: ______________________ Date: ______________

Hall: B Anticipated Run Date: 2006 PAC Approved Days: __________

Spokesperson: W. Brooks + 5 more Hall Liaison: ______________________
Phone: 757-269-6391
E-mail: brooksw@jlab.org

List all combinations of anticipated targets and beam conditions required to execute the experiment. (This list will form the primary basis for the Radiation Safety Assesment Document (RSAD) calculations that must be performed for each experiment.)

Condition No.	Beam Energy (MeV)	Mean Beam Current (μA)	Polarization and Other Special Requirements (e.g., time structure)	Target Material (use multiple rows for complex targets — e.g., w/windows)	Material Thickness (mg/cm^2)	Est. Beam-On Time for Cond. No. (hours)
1	5700	1.0	none	liquid hydrogen	1400	720

The beam energies, E_{Beam}, available are: $E_{Beam} = N \times E_{Linac}$ where N = 1, 2, 3, 4, or 5. E_{Linac} = 800 MeV, i.e., available E_{Beam} are 800, 1600, 2400, 3200, and 4000 MeV. Other energies should be arranged with the Hall Leader before listing.

HAZARD IDENTIFICATION CHECKLIST

JLab Proposal No.: ______________________ Date : ______________

(For JLab U/I Liaison Office use only.)

Check all items for which there is an anticipated need.

Cryogenics 4 beamline magnets ___ analysis magnets 1 target type: LH2 flow rate: 0 capacity: ___	**Electrical Equipment** ___ cryo/electrical devices ___ capacitor banks ___ high voltage ___ exposed equipment	**Radioactive/Hazardous Materials** List any radioactive or hazadorous/ toxic materials planned for use: ___ ___ ___ ___
Pressure Vessels ___ inside diameter ___ operating pressure ___ window material ___ window thickness **Special Target Materials** ___ * Helium (^{3}He) ___ Deuterium	**Flammable Gas or Liquids** type: ___ flow rate: ___ capacity: ___ **Drift Chambers** type: ___ flow rate: ___ capacity: ___	**Other Target Materials** ___ Beryllium (Be) ___ Lithium (Li) ___ Mercury (Hg) ___ Lead (Pb) X Tungsten (W) ___ Uranium (U) ___ Other (list below) ___ ___
Vacuum Vessels ___ inside diameter ___ operating pressure ___ window material ___ window thickness	**Radioactive Sources** ___ permanent installation ___ temporary use type: ___ strength: ___	**Large Mech. Structure/System** ___ lifting devices ___ motion controllers ___ scaffolding or ___ elevated platforms
Lasers type: ___ wattage: ___ class: ___ Installation: ___ permanent ___ temporary Use: ___ calibration ___ alignment	**Hazardous Materials** ___ cyanide plating materials ___ scintillation oil (from) ___ PCBs ___ methane ___ TMAE ___ TEA ___ photographic developers ___ other (list below) ___ ___	**General** Experiment Class: X Base Equipment ___ Temp. Mod. to Base Equip. ___ Permanent Mod. to Base Equipment 1 Major New Apparatus Other: ___ ___

LAB RESOURCES LIST

JLab Proposal No.: ____________ Date ____________

(For JLab ULO use only.)

List below significant resources — both equipment and human — that you are requesting from Jefferson Lab in support of mounting and executing the proposed experiment. Do not include items that will be routinely supplied to all running experiments such as the base equipment for the hall and technical support for routine operation, installation, and maintenance.

Major Installations *(either your equip. or new equip. requested from JLab)*

Install a 4-dipole chicane

Install a mechanism to position crystal array

New Support Structures:

Data Acquisition/Reduction

Computing Resources: Standard

New Software:

Major Equipment

Magnets: 4 dipoles

Power Supplies: Power supplies for dipoles

Targets: LH2 target, 20 cm long, 10 cm diameter

Detectors: Lead tungstate crystal array

Electronics: Electronics for above crystals

Computer Hardware:

Other:

Other:

Computing Requirements List

Proposal Title: Beyond the Born Approximation: A Precise Comparison of Positron-Proton and Electron-Proton Elastic Scattering in CLAS

Spokesperson: W. Brooks + 5 more **Experimental Hall:** B

Raw Data Expected

Total: 30 Tb **Per Year (long duration experiments only):** N/A

Simulation Compute Power (SPECint95 hours) Required: 3 million

On-Line Disk Storage Required: standard

Imported Data Amount from Outside Institutions: none

Exported Data Amount to Outside Institutions:w 20% of data set

Expected Mechanism for Imported/Exported Data: internet

Special Requirements

For example, special configuration of data acquisition systems) that may require resources and/or coordination with JLab's Computer Center. Please indicate, if possible, what fraction of these resources will be provided by collaborating institutions and how much is expected to be provided by JLab.

none

Beyond the Born Approximation: A Precise Comparison of e$^+$p and e$^-$p Elastic Scattering in CLAS

A Proposal to PAC26

J. Arrington*, X. Zheng
Argonne National Laboratory

F. Klein, D. Sober
The Catholic University of America

K. Joo*, M. Ungaro
University of Connecticut

B. A. Raue*, W. Boeglin, M. Moteabbed
Florida International University

A. Afanasev*, W. K. Brooks*†, V. D. Burkert, A. Deur, L. Elouadrhiri, D. W. Higinbotham, B. A. Mecking, W. Melnitchouk
Jefferson Lab

G.E. Dodge, C.E. Hyde-Wright, L. B. Weinstein*
Old Dominion University

and the CLAS COLLABORATION

(Dated: May 24, 2004)

A direct measurement of the two photon exchange contribution to lepton-proton elastic scattering is proposed. This process has been suggested to play an important role in explaining the discrepancy observed between two methods of measuring the proton's G_E/G_M ratio. A definitive test of this assertion is possible via a high precision comparison of e^+p and e^-p elastic scattering. The proposed measurement, which uniquely exploits the large acceptance of CLAS, may also influence the interpretation of other high-precision measurements including extractions of the small amplitudes in the N to Δ transition or the elastic form factors for few-body nuclei.

* spokesperson
† contact person

Contents

I. INTRODUCTION

The electromagnetic form factors are essential pieces of our knowledge of nucleon structure. However, the proton electric form factor, G_E, is currently unknown by a factor of three at $Q^2 = 5.6$ GeV^2 [1–5]. Until the cause of the discrepancy is fully understood, the uncertainty in the form factors affects the theoretical and experimental understanding of several measurements.

Theoretically, it is unclear what value of G_E should be used to compare to lattice calculations or models of proton structure. Theoretical corrections needed to resolve the G_E discrepancy may also be important for interpreting other electron scattering measurements. Experimentally, it is unclear what value of G_E should be used as input in the analysis of experiments from $(e, e'p)$ to color transparency, especially at high Q^2 or when studying the ε-dependence. While the discrepancy in G_E is largest at higher Q^2, there may still be significant effects even below $Q^2 = 1$ GeV^2, where the elastic form factors are needed as input in precision measurements of nuclear structure from $A(e, e'p)$ measurements.

The goal of this experiment is to resolve the discrepancy between the Rosenbluth and polarization transfer measurements of G_E. It is currently believed that two-photon exchange (TPE) effects are the cause of the discrepancy. We will measure $\frac{\sigma(e^-p)}{\sigma(e^+p)}$, the ratio of elastic electron-proton and positron-proton scattering, as a function of ε and Q^2, in order to directly extract the TPE corrections to elastic scattering for $0.5 < Q^2 < 2.5$ GeV^2. This will provide important constraints for models of the TPE effects.

The uncertainty in G_E arises from a discrepancy between Rosenbluth separations of the unpolarized cross section [1, 4, 5] and polarization transfer measurements [2, 3]. Assuming one photon exchange (first Born approximation, see Fig. 1), the cross section can be written as

$$\frac{d\sigma_B}{d\Omega} = C_B(Q^2, \varepsilon)\left[\tau G_M^2(Q^2) + \varepsilon G_E^2(Q^2)\right] \tag{1}$$

where the virtual photon polarization $\varepsilon = [1 + 2(1 + \tau)\tan^2(\theta_e/2)]^{-1}$, $\tau = Q^2/4M^2$ and C_B is a known kinematic factor. By varying ε, the Rosenbluth measurements separate R_L, which is proportional to G_E^2, from R_T, which depends on both G_E and G_M. These measurements yield $G_E \approx G_M/\mu_p \approx G_{Dipole}$ for Q^2 up to 5–10 GeV^2. Recent "Super-Rosenbluth" measurements, where the recoil proton (rather than the scattered electron) was detected, have confirmed the original Rosenbluth measurements with much smaller systematic uncertainties. The form factors have also been measured in polarization transfer experiments using $(\vec{e}, e'\vec{p})$. In the Born approximation, the ratio of the transverse and longitudinal recoil proton polarizations P_t/P_l is directly proportional to G_E/G_M. These experiments show a significant decrease in G_E compared to G_M as Q^2 increases, with G_E/G_M a factor of three below the Rosenbluth results at $Q^2 = 5.6$ GeV^2.

Two-photon exchange (TPE) contributions (see Fig. 1 (e) and (f)) might be able to explain the discrepancy [6]. Because the contribution of G_E to the cross section is kinematically suppressed compared to G_M for large 4-momentum transfers, $Q^2 > 1$ GeV^2, a small (5–8%) ε-dependent TPE correction to the cross section can explain the large difference between the polarization and Rosenbluth extractions of G_E [6, 7].

If a TPE contribution to the cross section is responsible for the entire difference between Rosenbluth and polarization transfer measurements, the effect must be approximately linear in ε, result in a 5–8% change in the slope of the Rosenbluth cross section plotted vs. ε, and depend only weakly on Q^2. Figure 2 shows the values of $\mu_p G_E/G_M$ one would obtain from a Rosenbluth separation, assuming that the polarization transfer value of $\mu_p G_E/G_M$ is correct and adding a phenomenological fit to the TPE correction with a linear ε-dependence and a weak

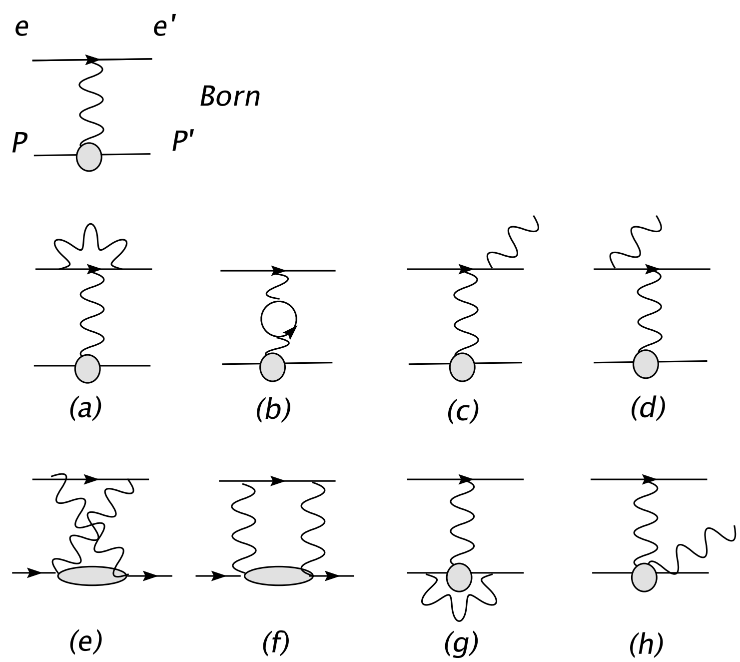

FIG. 1: Feynman diagrams for the elastic electron-proton scattering, including the 1st-order QED radiative corrections. Diagrams (e) and (f) show the two-photon exchange terms, where the intermediate state can be an unexcited proton, a baryon resonance or a continuum of hadrons.

Q^2-dependence (given in the figure) to the cross section measurements. With these simple parameterizations for the two-photon contribution, the observed slope is consistent with the Rosenbluth measurements of the form factor ratio [8] over the entire Q^2 range where data are available.

Calculations [9–11] of the TPE diagrams (diagrams (e) and (f) in Fig. 1) suggest that these effects may indeed be large enough to explain the discrepancy. However, these calculations require model-dependent treatment of the hadron structure and are therefore not yet sufficiently understood to be applied to the data as additional radiative corrections. The TPE explanation is also supported by a reexamination of positron-proton and electron-proton scattering [12]. The dominant TPE effect on the cross section comes from the interference between one-photon and two-photon exchange, which changes sign when the charge of the beam or target changes. The e^+/e^- cross section ratio data show a linear ε-dependence of $5.8 \pm 1.8\%$, with the largest effects at small ε. However, there are only seven data points at $\varepsilon < 0.5$ and only one of those is at $Q^2 > 1$ GeV^2. In addition, the statistical errors are typically at least 5%.

We propose to extend these e^+/e^- cross section ratio measurements to low ε and moderate Q^2 values with high statistical precision. We will use a 5.7 GeV electron beam incident on the CLAS tagger to create a real photon beam. The photon beam will strike a converter, creating e^+/e^- pairs which enter a 4-dipole chicane magnet. These pairs will be separated from the photon beam by two dipole magnets, and the photon beam will be stopped; the lepton beams will then be recombined by two more dipole magnets, and will proceed to impinge on a single hydrogen target in the center of CLAS. We will then detect the recoil protons and the scattered leptons in the CLAS spectrometer. In order to reduce systematic errors, we will periodically

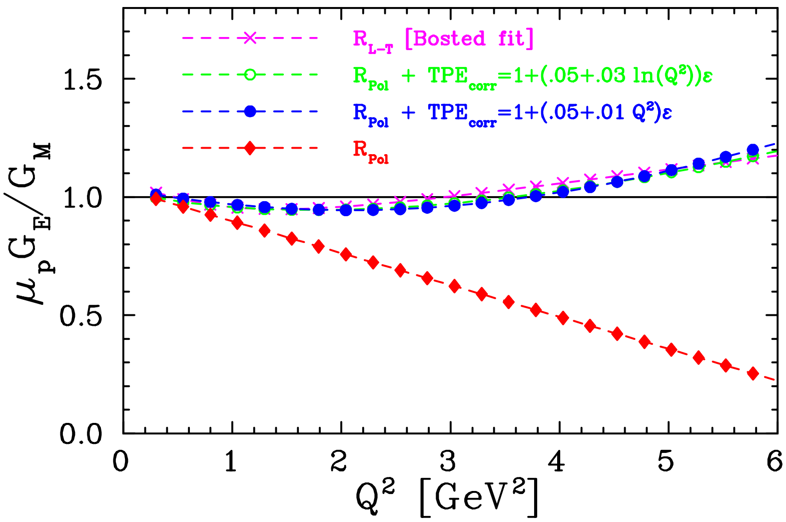

FIG. 2: The value of $\mu_p G_E/G_M$ that would be measured by the Rosenbluth separation under various conditions using the actual value of $\mu_p G_E/G_M$ from the polarization transfer experiments. The diamonds show the results of the Rosenbluth measurement if there are no TPE effects. The open and closed circles show the results of the Rosenbluth measurement if there are small (few percent) TPE corrections as shown in the legend. The crosses show a fit to the actual Rosenbluth results. [8]. Note that it only takes a few percent TPE contribution to explain the difference between the polarization and Rosenbluth results.

flip the polarity of the e^+/e^- magnet chicane and of the CLAS toroidal magnet. By doing this, we will simultaneously measure the cross section asymmetry for e^+ and e^- scattering from the proton to determine the magnitude of two-photon exchange effects with high statistical and systematic precision.

Since two-photon exchange could change the measured value of G_E by a factor of three, an experimental determination of its contribution becomes very important. The proposed measurements will allow us to determine the effects of TPE on electron-proton elastic scattering and resolve the ambiguity presently surrounding the charge form factor of the proton.

Section II will discuss the theoretical considerations in more detail and section III will present the experimental method.

II. SCIENTIFIC MOTIVATION

A. Overview

The Rosenbluth formula for elastic ep-scattering [13] was derived using the one-photon exchange approximation. Measurements of nucleon electromagnetic form factors and experiments on parity-violating electron scattering are based on the same approximation. When electron scattering data are analyzed, radiative corrections must be applied to take into account higher-order processes. These processes include vertex corrections (a and g in Fig. 1), vacuum polarization or loop diagrams (b), the emission of a real photon from the electron or proton (c,d,h), two-photon exchange (e and f), as well as higher-order (multi-photon) terms. Many of these corrections involve only lepton-photon vertices (electron bremsstrahlung, electron vertex, and loop diagrams), and can be calculated exactly in QED or, in the case of quark loops, determined from $e^+ - e^-$ annihilation data. Terms that involve the proton include the proton vertex correction, two-photon and multi-photon exchange, and proton bremsstrahlung. These terms cannot be calculated exactly and must be estimated or measured by other techniques. Of these terms, the greatest uncertainty is associated with the two-photon exchange. The proton vertex correction is quite small except for extremely high Q^2 and ϵ-independent at fixed Q^2, while proton bremsstrahlung is fairly well understood due to a low-energy theorem. Exchange of more than two hard photons is a higher order process, and is expected to be another order of α_{em} smaller than the two-photon and other radiative correction terms. The effect of multiple *soft* photon exchange, often referred to as Coulomb corrections (CC), enter at the same order as the primary radiative corrections after resummation, and so are also important to consider.

Two-photon exchange effects, referred to as 'dispersive effects,' have been seen before in electron scattering on heavier nuclei. They showed up typically in the energy dependence of form factors measured in elastic electron scattering [14] and in discrepancies between nuclear charge radii measured with muonic atoms and with elastic electron scattering [15]. They were studied in several different ways, including 'forbidden transitions' in electron scattering (e.g.: $^{16}\mathrm{O}(e,e')$ $0^+ \to 0^-(10.9)$ MeV[16]), and the comparison of electron and positron elastic scattering from $^{12}\mathrm{C}$ [17]. However, it was generally assumed that these few-percent effects would be much smaller on the proton ($Z = 1$) than on larger nuclei ($Z \gg 1$).

The formalism developed by Mo and Tsai [18, 19] is commonly used to apply radiative corrections. However, these corrections include only the infrared divergent contributions from the two-photon exchange diagrams (necessary to cancel the IR-divergent terms in the interference between proton and electron bremsstrahlung), and neglect contributions from multiple soft photon exchange (Coulomb corrections). Both the TPE and CC contributions are of $\mathcal{O}(\alpha_{em})$ with respect to the Born amplitude, and are therefore important to include, especially for Rosenbluth form factor measurements that require a high-precision extraction of the ε-dependence of the cross section. These terms cannot be calculated in a model-independent way, and so direct measurements of such corrections must be made to allow unambiguous interpretation of electron-proton scattering measurements with an accuracy better than 1%.

Fortunately, the contribution of two-photon exchange and Coulomb corrections can be measured directly without referring to models of nucleon structure. This is possible due to the fact that the TPE corrections (and CC) have opposite signs for scattering cross sections of positrons vs. electrons, producing a measurable charge asymmetry in $R = \sigma(e^+)/\sigma(e^-)$, where $\sigma(e^+)$ and $\sigma(e^-)$ denote elastic cross sections of positron- and electron-proton scattering, respectively.

The radiative corrections for electron and proton scattering are discussed in more detail in Section II C. However, the radiative corrections can be divided into two categories: those whose sign is independent of charges of the incident particles, and those whose sign depends on the charges of the particles. The "standard" radiative corrections are all independent of the sign of the lepton, except for the interference term between electron (positron) bremsstrahlung and proton bremsstrahlung that is regularized by a corresponding infra-red term from TPE. The effects of TPE and CC have the opposite sign for electrons and positrons. Therefore, after applying the standard radiative corrections, including the interference between electron and proton bremsstrahlung, the TPE radiative correction to the cross section can be written as

$$\sigma(e^\pm) = \sigma_{Born}(1 \mp \delta_{2\gamma}), \tag{2}$$

where $\delta_{2\gamma}$ is a TPE correction. This yields a charge asymmetry of:

$$R = \frac{\sigma(e^+)}{\sigma(e^-)} \approx 1 - 2\delta_{2\gamma}. \tag{3}$$

Thus, it is evident that the charge asymmetry of Eq. 3 is a direct and model-independent measure of the TPE effect for the elastic electron-proton scattering.

B. Estimates of TPE effects

1. Calculations

Extending earlier work by Maximon and Tjon [20] on the nucleon elastic contribution to the box diagram (diagrams (e) and (f) in Fig. 1), Blunden, Melnitchouk and Tjon [9] included form factors in the loop integrals to estimate the impact of hadronic structure on the two-photon exchange calculation. Using simple monopole form factors, the structure effects were found to give rise to a significant ε-dependence, which accounted for about half of the difference between the Rosenbluth and polarization transfer measurements. With the use of realistic form factors, the effect was found to increase somewhat [21], making the discrepancy even smaller. In addition to the nucleon elastic contribution, one expects excitation of nucleon resonances, such as the Δ, to become relatively more important at higher Q^2 values, and these are currently being evaluated [21].

The Axial-VMD model, originally proposed by Drell and Sullivan [22], was recently revised by Afanasev [10]. In this model, the entire strength of the TPE effect is attributed to exchanges of axial mesons such as $a_1(1260)$ and $f_1(1285)$, which are the lightest mesons whose coupling conserves electron helicity and has the positive charge parity of the 2-photon exchange. The axial meson coupling was obtained from a fit to the difference between Rosenbluth and polarization measurements of the ratio G_E/G_M. This model predicts corrections that are small at large ε, but which can become significant at low and moderate ε values.

A calculation at the quark-parton level in the factorized approximation was performed by Afanasev, Brodsky, and Carlson [10]. It does not use any fitting parameters, and assumes a fixed value $\langle x \rangle = 1/3$ for the fraction of (longitudinal) momentum of the nucleon carried by the struck quark. Like the Axial-VMD fit, it brings Rosenbluth and polarization data on G_E into qualitative agreement, but its dependence on the electron scattering angle (or ε) at fixed Q^2 is rather different. This calculation yields a nearly linear ε-dependence over most of the ε range, that results in about the same correction to the Rosenbluth slope as the model [9], but predicts larger effects for smaller values of $\varepsilon < 0.2$ The TPE effect in this model is Q^2–independent.

It is interesting to note that the quark-parton models of the TPE effect predict a negative sign of the charge asymmetry at large values of ε and a change of sign to positive values around ε= 0.4 to 0.6. On the other hand, the models using only hadronic degrees of freedom, *i.e.*, the elastic contribution [9] and Axial-VMD [10] do not predict a change of sign as a function of ε.

Figure 3 shows the high Q^2 SLAC data on charge asymmetry [23] plotted against the predictions of the models described above. All of these models yield TPE corrections that improve the agreement between the Rosenbluth and polarization extractions of the form factors. They all predict a relatively weak dependence on Q^2, at least for large Q^2 values, but they predict different dependences on the electron scattering angle (or ε) at fixed Q^2 values. Therefore the proposed measurement, besides giving a definite answer to the problem of the discrepancy between Rosenbluth and polarization data, will also constrain the models of TPE effects that depend on nucleon structure.

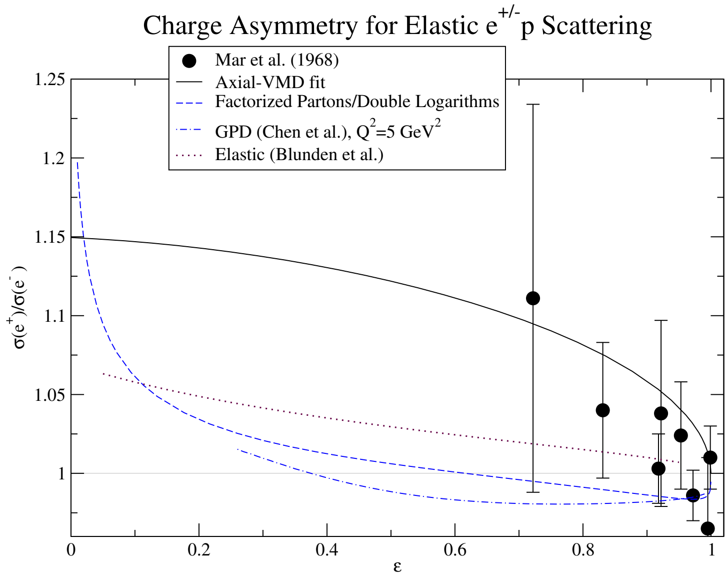

FIG. 3: The ratio of the e^+p differential cross section to the e^-p differential cross section as a function of ε.

2. *Phenomenological estimates*

These calculations give us some guidance as to the size and form of the TPE corrections. However, they yield different quantitative results and some are not expected to be valid at low Q^2 values. Therefore, we also try and estimate the size of expected TPE effects at low Q^2 by analyzing the Q^2-dependence of the discrepancy itself, as well as the existing positron data at low Q^2.

Guichon and Vanderhaeghen [6] parameterized the two-photon exchange (TPE) amplitude in the most general form and fitted the discrepancy between polarization transfer and Rosenbluth measurements in order to evaluate the magnitude of the largest contribution of the TPE terms. They discussed the possible angular dependence of the correction and concluded that the TPE effect is up to about 3.5% at the amplitude level. Their analysis predicts a cross section dependence that is approximately linear with ε, and which yields an ε-dependence to the electron cross section of ∼3–5% and thus a 6–10% effect on the positron to electron ratio in the Q^2 range of this proposal.

A more detailed analysis [24], using the same generalized form factors but including constraints from the positron data, allows the extraction of additional TPE amplitudes. These additional amplitudes have smaller effects on the discrepancy but are still important in the cross section and positron-to-electron comparisons. The two-photon amplitudes are extracted from a fit to the Rosenbluth/polarization-transfer discrepancy, with the constraint that the effect on the cross section be small for $\varepsilon \to 1$ where the existing positron data set reasonable limits on the TPE effects.

Once these amplitudes have been fit to the data, we can use them to predict the expected positron to electron ratio for this proposal. The uncertainties on the amplitudes, and thus the prediction, are relatively large and the amplitudes are only well constrained by the data for $Q^2 \gtrsim 1.5$ GeV^2. However, by comparing to the existing very low Q^2 positron data, we can see that the extrapolation to low Q^2 values yields reasonable results. Figure 4 shows the existing

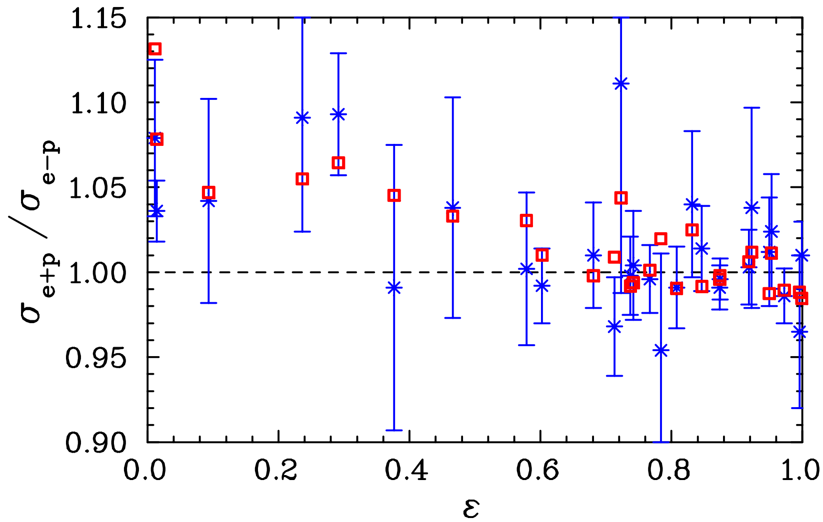

FIG. 4: The existing $\sigma(e^+)/\sigma(e^-)$ data (blue 'x') compared to the predicted value based on the two-photon amplitudes extracted as described in the text (red squares).

positron-to-electron data compared to the expectation based on the above analysis. At large ε, the fit is constrained to yield $R \approx 1$. However, the lower ε data is not used to constrain the fit, and so the agreement between the data and the extracted amplitudes gives us confidence that these amplitudes provide a reasonable starting point for estimating the size of the signal that we expect to observe in this measurement.

Based on the amplitudes extracted from this analysis, we expect that for the region where we will have high statistics, the ε-dependence of the ratio will vary from $\sim$6% for $Q^2 = 0.5$ GeV^2 to $\sim$10% for $Q^2 = 2.0$ GeV^2.

C. Radiative Correction Details

The extraction of the elastic form factors requires extraction of the Born cross section. This means that corrections must be applied to the measured cross sections to correct for the additional diagrams in Fig. 1, as well as higher order terms. Most of these corrections are well understood (exactly calculable in QED) and taken care of in standard prescriptions for radiative corrections [25]. Most of these terms are identical for electron- and positron-proton scattering, and so comparison of electron- and positron-proton scattering is a sensitive way to test the terms that are not as well understood theoretically. Early comparisons of electron- and positron-proton scattering indicated that the two-photon exchange terms were very small ($\lesssim$1%). In this comparison, the only portion of the standard radiative corrections that changes sign is the interference between electron (positron) and proton bremsstrahlung, which is well understood, and so the test is extremely sensitive to TPE (and multi-photon) effects.

Let us demonstrate the relation of the charge asymmetry to the TPE correction to the cross section. The amplitude of elastic ep-scattering with an accuracy of α_{em}^2 can be written as

$$A_{ep\to ep} = e_e e_p A_{Born} + e_e^2 e_p A_{e.br.} + e_e e_p^2 A_{p.br.} + e_e^2 e_p^2 A_{2\gamma}, \tag{4}$$

where the electron (e_e) and target (e_p) charges are written explicitly, and the amplitudes $A_{Born}, A_{e.br.}, A_{p.br.}$ and $A_{2\gamma}$ respectively describe one-photon exchange, electron bremsstrahlung, proton bremsstrahlung and two-photon exchange. Note that radiative corrections such as vertex corrections and vacuum polarization do not contribute to the charge asymmetry and therefore are not included here. Squaring the amplitude in Eq. 4 and keeping the corrections up to the order α_{em} that have odd powers of electron charge, we have

$$|A_{ep\to ep}|^2 = e_e^2 e_p^2 [|A_{Born}|^2 + e_e e_p A_{Born} 2Re(A^*_{2\gamma}) + e_e e_p 2Re(A_{e.br.} A^*_{p.br.})], \tag{5}$$

where the notation Re is used for the real part of the amplitude.

Corrections that have an even power of electron charge, including the largest correction from electron bremsstrahlung, do not lead to any charge asymmetry. The last term in the above expression describes interference between electron and proton bremsstrahlung. Its infrared divergence exactly cancels the corresponding infrared divergence of the term $A_{Born}Re(A^*_{2\gamma})$, making the QED description of the ep-scattering self-consistent. This interference effect for the standard kinematics of elastic ep-scattering experiments is dominated by soft-photon emission and results in a factorizable correction already included in the standard approach to radiative corrections [18, 19].

Therefore, after correcting for the interference between electron and proton bremsstrahlung, the radiative correction to the electron scattering cross section that leads to charge asymmetry comes from TPE (Eq. 5).

While we discuss TPE and CC as two independent corrections, this is a somewhat artificial separation. While we define CC as multiple soft-photon exchange, it of course has contributions from the soft part of two-photon exchange, and the effect is double-counted if these corrections are calculated and applied independently. However, it is the combined effect that is important in the Rosenbluth separation, and it is the combined effect that is measured in the comparison of electron- and positron-proton scattering. So while there are theoretical ambiguities in separating these effects based on the proposed measurements, these measurements provide exactly the corrections that are necessary when comparing Rosenbluth (cross section) measurements of the form factors to polarization transfer measurements.

III. EXPERIMENTAL METHOD

A. Overview

The experimental method proposed begins with an electron beam incident on the Hall B tagger radiator. The tagger magnet will sweep the electron beam into the tagger beam dump below the Hall B floor. The tagging detectors will not be used at all, except possibly for calibration runs.

The photon beam thus produced propagates to a photon collimator followed by a sweeping magnet, and then impinges on a converter that produces e^+e^- pairs. These pairs are separated by two dipole magnets, and at that point the photon beam is stopped by a photon blocker. The leptons are then recombined in two more dipole magnets, pass through a multi-component shielding structure, and interact with a large-diameter hydrogen target in the center of CLAS. Elastic scattering events are identified by a series of cuts such as coplanarity and correlations between polar angles and momenta. Once identified, all relevant quantities (such as incident lepton energy) can be calculated.

The systematic errors in this method are very small because of the symmetry of the reaction and the experimental apparatus. The capacity to simultaneously measure a wide range in ε is due to the large acceptance of CLAS; large acceptance also permits the use of a beam of only a few hundred pA to achieve excellent statistical errors in a modest period of time. Control over the asymmetry in the incident flux of positrons and electrons is maintained by a specialized direct measurement at low rates, and continuous monitoring at high rates. Experimental backgrounds are present and non-negligible, but are held to a manageable level by careful placement of shielding materials in a strategy steered by numerous simulations.

The following sections contain detailed discussions of various aspects of the proposed experimental technique. A description of the equipment and the scheme to measure the incident flux of leptons will be followed by a description of the triggering method and data analysis. Next come discussions of experimental backgrounds and systematic errors. Finally, an estimate of counting rates will be given, and an approach to the physics analysis will be presented.

B. Description of experimental equipment

The measurement is to be carried out using the CEBAF Large Acceptance Spectrometer, CLAS, in Hall B. The spectrometer and triggering system are all to be used in their standard configurations. A small facility for producing and monitoring positron and electron beams will, however, need to be constructed.

A drawing of the beamline is shown in Fig. 5. The electron beam from the accelerator ($\sim$1μA) impinges on a 5% X_o radiator located in the conventional position in front of the tagger magnet (not shown). This magnet will be energized to deflect the primary beam to the tagger dump. (Both the beam current and the radiator thickness are significantly greater than

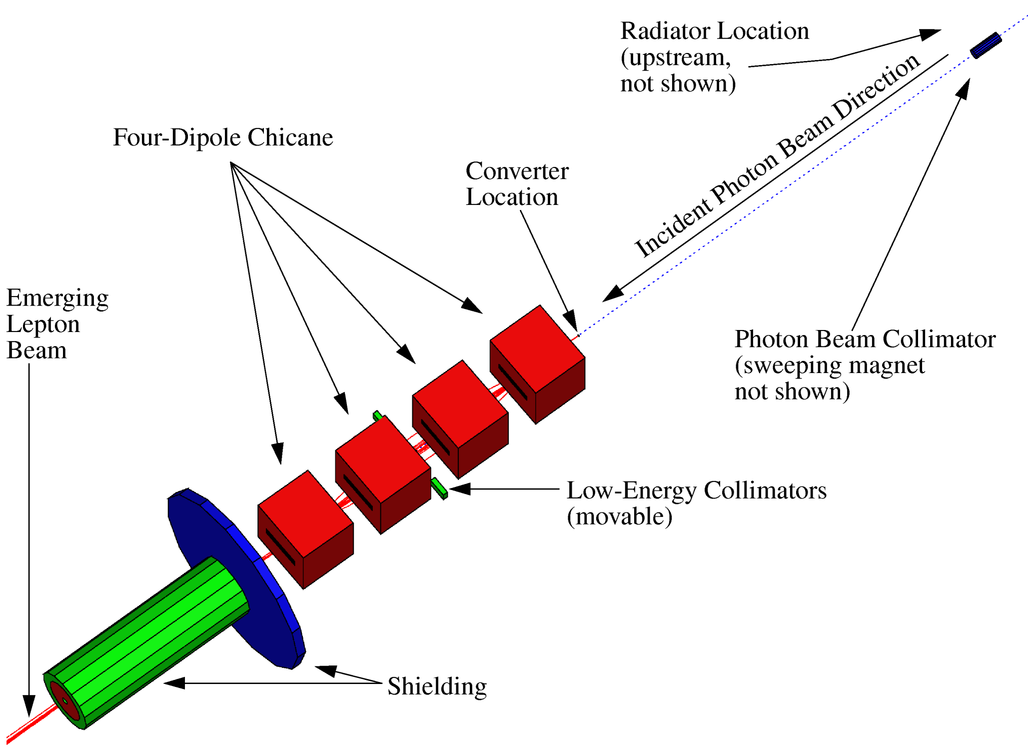

FIG. 5: An overview of the beamline devices that produce the lepton beam entering CLAS. The depicted portion of the beamline is approximately 10 m in length.

in normal operation, therefore, use of the tagging detectors is precluded.) Although this dump has only been used for low-power deposition to date (<800 watts), it was conservatively designed to accommodate 10 kW when outfitted with air cooling, and it has a functioning temperature monitoring system. The photon beam propagates along the beamline axis, passing through an existing 2 mm diameter, 12 inch long nickel collimator and an existing sweeping magnet (not shown) presently used as the Primex pair spectrometer magnet. The initial beam energy has been chosen to be large so that the highest average Q^2 is reached; it has the additional benefit that the natural divergence of the photon beam is minimized, so that less collimation is required.

The collimated photon beam then passes through a 2% X_o converter, producing electron-positron pairs. These pairs enter a chicane consisting of four dipole magnets. These can be seen in more detail in Fig. 6 and Fig. 7. The chicane serves to spatially separate the positron and electron beams and then recombine them. In the region where the beams are separated, the remaining photon beam is absorbed in a "photon blocker", a 1 cm by 10 cm cylinder of tungsten. Either lepton beam can also be fully or partially blocked by moving in two "low-energy collimators". When the low-energy collimators are partially inserted, they serve to remove the lower-energy component of the lepton beams, so as to limit the luminosity at energies that are too low to be of interest. The photon blocker can be seen in the center of Fig. 7 as a small blue rectangle, while the low-energy collimators are indicated by larger green rectangles nearby. In this figure the trajectories of positrons and electrons are indicated for momenta from 0.5 GeV to 5.7 GeV; the 0.5 GeV leptons are blocked in this particular figure by the low energy collimators. A 5 kG field has been used in each of the four dipole magnets.

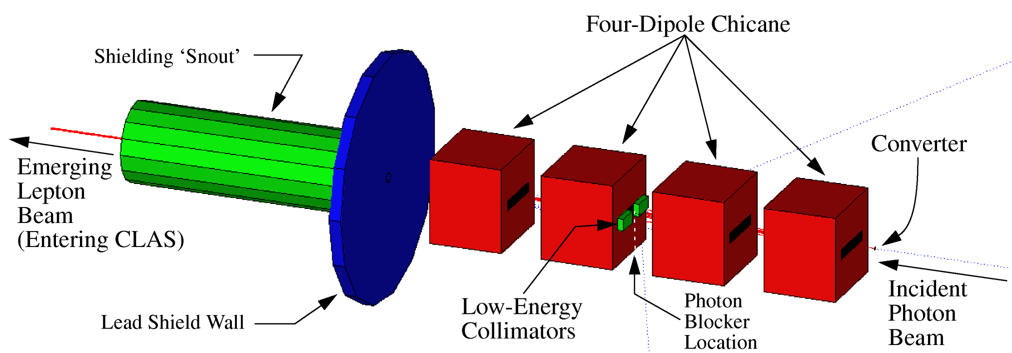

FIG. 6: A closeup view of the magnet chicane and shielding.

Leptons of the lowest momenta cannot contribute kinematically to the range of Q^2 and ε of interest in this experiment, and therefore they are blocked by the low-energy collimators. Simulations have suggested that an approximately optimal configuration is achieved by blocking 0.5 GeV leptons and below; this will be refined in the final design of the experiment. During flux measurements, the low-energy blockers will be moved in to block all of the electrons, or alternatively all of the positrons, to study the energy dependence of the flux of each separately. The flux will be measured at the target location, and also monitored continuously in front of the second dipole in the chicane. Flux monitoring is described in detail in Sec. III C.

Following the chicane is a lead shield wall with a small tungsten collar 2" in inner diameter in the center. Simulations have indicated that an outer diameter of 2 m is sufficient to block most of the background generated upstream. A more challenging component to remove are the leptons

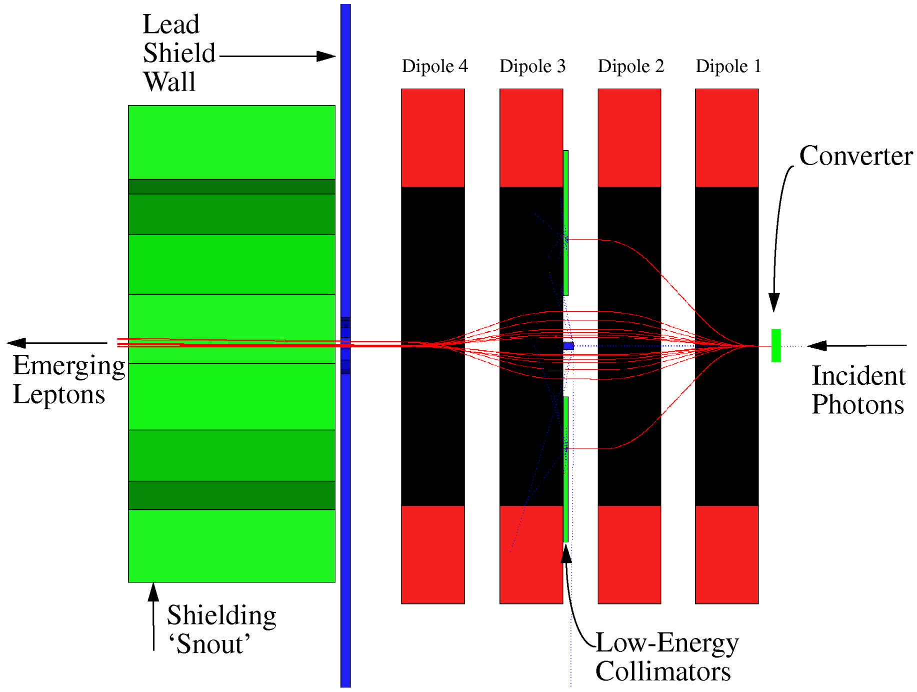

FIG. 7: Trajectories of the leptons through the chicane. The vertical scale is six times greater than the horizontal scale. The leptons shown range from 0.5 to 5.7 GeV. Each dipole has a 5 kG field.

with a trajectory that is similar to the lepton beam. These primarily come from scraping off the low-energy collimators, although they can come from elsewhere as well. Simulations have shown that these have wider angular dispersion and typically have energies of 100-200 MeV. Therefore, a long 'snout' shield follows the lead wall. The inner portion of the snout is made of carbon, to take advantage of dE/dx losses without inducing further showers, while the outermost portion is made of lead.

A single cryotarget will be used. Because of the beam divergence, the target will be larger in diameter than what is normally employed for electron beams. The outgoing lepton beam has an angular divergence that is due to a combination of the bremsstrahlung process, the pair production process, and multiple scattering in the converter and radiator. Simulations have shown that the lower-momentum leptons have a somewhat broader angular distribution than the higher-momentum leptons, suggesting that multiple scattering in the converter is the most significant effect. A 10 cm diameter target will intercept all but a few percent of the leptons. This is comparable in size to targets that have been used in early photon beam experiments in CLAS, and therefore presents no new technical challenges.

C. Flux Measurement and Monitoring

Both absolute and relative measurements of the electron and positron fluxes will be performed. The relative flux will be measured continuously throughout the experiment and tied to an absolute flux measurement done prior to taking $e^{\pm}+p$ elastic data. The absolute flux measurement will be done by moving a position-sensitive calorimeter into the beam just upstream of the target location. Running at low beam currents, this device will enable us to measure the rate and energy distribution of electrons and positrons at the target. The flux at the target for low beam currents will be cross calibrated to the flux of unused low-energy ($E < 0.5$ GeV) leptons measured with a separate set of detectors located in the dispersed region in front of dipole 2. The flux of the unused low-energy leptons should simply scale with the primary electron beam current. Therefore, continuously monitoring this low-energy flux during the experiment should enable us to know the flux at the target for production currents.

The device we envision for the energy profile measurement at the target is a segmented lead tungstate ($PbWO_4$) calorimeter with a position-sensitive detector in front (see figure 8). The calorimeter consists of 120 crystals each with a cross-sectional area of 2×2 cm^2 and a length of 16 cm (18 radiation lengths). The total cross-sectional area of the calorimeter was chosen so that each electromagnetic shower that falls within the target radius (indicated by the smaller circle) deposits 99% of its energy within the calorimeter. 99% of the energy of an electromagnetic shower is contained within a cylinder of 3.5 Moliére radii (R_M) centered on the incident particle [26]. R_M for $PbWO_4$ is 2.0 cm meaning that we need an additional 7.0 cm beyond the edge of the target, or a total diameter of 24 cm (indicated by the larger circle), in order to contain 99% of the shower. We can obtain 96% containment with a total diameter of 20 cm (indicated by the middle circle). This can be covered by 80 crystals.

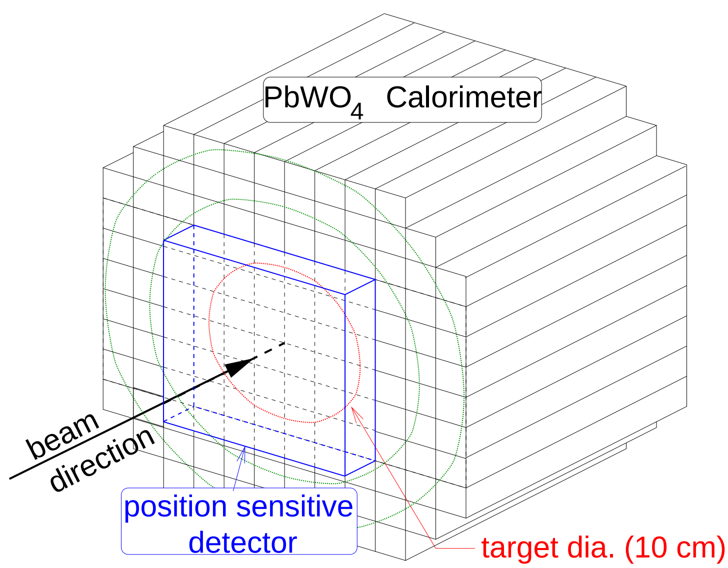

FIG. 8: $PbWO_4$ calorimeter and position-sensitive detector used to measure the distribution of lepton energy near the target location.

The position-sensitive detector in front of the calorimeter will tell us the location of the incident particle on the face of the calorimeter. The detector will be likely be either a pair of crossed microstrip detectors or wire chambers. 1 mm position resolution is easily achievable and sufficient for our purposes. The active area of the detectors will be slightly larger than 12×12 cm^2–sufficient to cover an area slightly larger that-n the target.

Previous studies [27] have shown that an energy resolution of $\sigma_E/E < 2\%$ can be obtained for an electron energy of 1 GeV and $\sigma_E/E < 0.9\%$ for 5 GeV electrons. This was done using gain-stabilized phototubes and also required controlling the temperature of the crystals to within $\pm 1^\circ$C. We can calibrate our calorimeter by illuminating it with particles of known energy and measuring the response of each element as a function of incident particle position. The range of energies at which we calibrate will match the lepton energies of the experiment–0.5 to 5.0

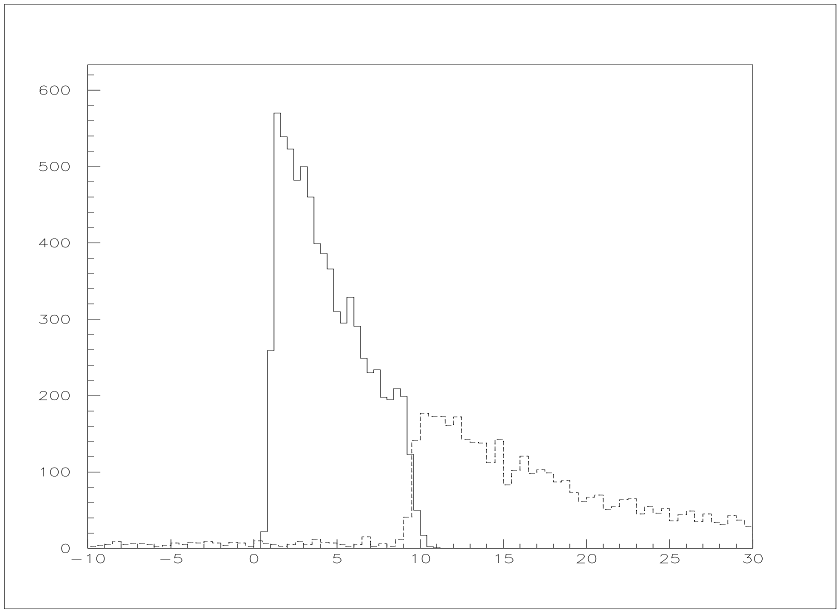

FIG. 9: Distribution of leptons in the horizontal direction perpendicular to the beam. The dashed histogram is for leptons of energy from 1 MeV to 0.5 GeV while the solid histogram is for leptons greater than 0.5 GeV. A vertical cut of ± 0.5 cm has been applied.

GeV. The energy calibration can be done with tagged photons. A center-of-gravity technique will enable a position reconstruction to within approximately 2–3 mm[27].

The flux of unused low-energy leptons in the dispersed region in front of dipole 2 will be continuously monitored. At this location along the beamline, leptons with an energy of more than 0.5 GeV are largely within 10 cm of the central axis of the beam while leptons with an energy of less than 0.5 GeV continue beyond 10 cm (see figure 9). A detector placed at $x > 10$ cm in both the positron and electron beams can then be used to monitor the relative rates of positrons and electrons. Changes in the position of the lepton beams would be seen as a change in relative rates in the two monitoring detectors.

The detectors we envision for relative flux monitoring are single quartz rods Cerenkov counters–one or more in each beam–instrumented with a fast photomultiplier tube as shown in figure 10. Quartz has an index of refraction of 1.47 resulting in Cerenkov radiation for all electrons and positrons of interest. This index of refraction also results in total internal reflection for the Cerenkov radiation and thus excellent light collection efficiency. In addition, quartz is radiation hard [28] and should stand up well over the course of the experiment despite the high particle flux; we expect rates in these detectors on the order 10^7 Hz. With a fast PMT we should be able to count individual leptons. This is preferable to integrating PMT signals in that small difference in detector response to different charges will be minimized.

An absolute calibration of the flux monitoring detectors can be tied to the measurement of the flux at the target using the $PbWO_4$ calorimeter. With one of the beams blocked off, the flux at the target can measured and compared to the rate in the monitoring detector. The roles of the beams can then be reversed and the other monitoring detector calibrated. It is likely that measurements at different beam currents will be necessary to verify scaling of the e^+/e^- fluxes. The sum of the rates in each of the quartz Cerenkov detectors will be proportional to the rate on the target. The ratio of the left and right quartz Cerenkov detectors will give us a continuous monitor of the relative e^+/e^- rates.

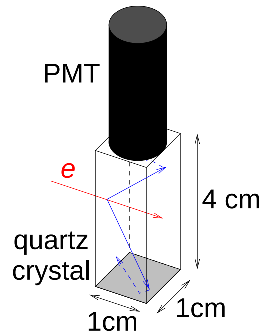

FIG. 10: Flux monitoring detector consisting of a single quartz rod and one PMT. Blue lines indicate the Cerenkov cone. The bottom surface is mirrored to improve light collection efficiency.

D. Triggering

The usual single-electron trigger employed by CLAS is not appropriate for this measurement; this trigger, based on the Cerenkov counter and electromagnetic shower calorimeter, would miss electrons and positrons at larger angles, severely limiting the coverage in ε. A further reason not to use the conventional trigger is that it may be biased by the Cerenkov counter, since that device has a slightly different efficiency for out-bending and in-bending tracks.

Instead, a trigger designed to detect $e^{\pm} + p$ coincidences will be used. This will require two charged tracks in opposite sectors and will be constructed by requiring hits in time-of-flight counters in opposite sectors in addition to a Level 2 (drift chamber) trigger in the same sectors. Other prescaled triggers may also be useful. The standard CLAS trigger system is adequate to fulfill these requirements.

Plots showing the kinematic correlations for the proposed measurement are given in Fig. 11.

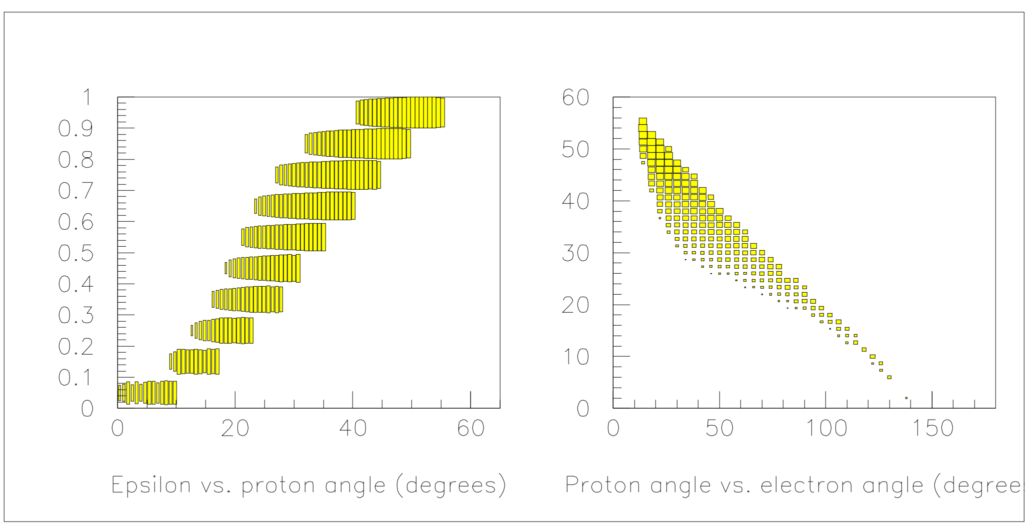

FIG. 11: In the left panel is shown the correlation between epsilon and the proton angle; the lower limit of epsilon is approximately 0.1 due to the proton acceptance in CLAS for normal torus polarity. The right panel shows the correlation between the proton angle and the electron angle. Both plots have logarithmic z axes.

E. Data Analysis

One example of how the data analysis chain might proceed is given in the following. The first criteria to be applied is to select events with only two hit-based tracks. The next requirement, that the tracks be co-planar and in opposite sectors, will strongly favor elastic scattering. Vertex times can be computed in two hypotheses for lepton/proton identification, and the correct vertex time difference will be consistent with zero. The resolution should be more than adequate to identify the lepton of the pair using this method. In addition, dE/dx in the time of flight counters (compared to the momentum from hit-based tracking) can provide further information to help identify the proton, without biasing the positron/electron selection.

Once the lepton is tentatively identified, its vertex time can be used to provide an event start time for time-based tracking, or, alternatively, the proton can be used to provide the event start time. Once time-based tracking has been performed, one can perform a tighter $\Delta\phi$ cut to ensure co-planar kinematics. At that point, one can assume that elastic scattering is the correct process, and can then calculate the beam energy and various kinematics using any combination of two variables of measured electron and proton kinematics. By comparing the measured and calculated values, one can achieve further background reduction by cutting out unphysical events. The ultimate analysis at this stage would be to use kinematic fitting to get the most consistent set of parameters and the cleanest identification of elastic scattering. Because the charged particle *angle* measurement is almost entirely determined by the Region I drift chamber (before any bend in a magnetic field), three of the four kinematic parameters measured (of which only two are independent) are insensitive to whether the lepton is a positron or electron; thus the comparison of the two can be performed very accurately.

1. *Reconstruction of existing CLAS data*

To demonstrate the ability of CLAS to perform such a data selection, we performed an analysis for data from the E1C run period that were taken in 1999 with electron scattering off a proton target. We considered two data sets for this analysis. The first data set is with $E_{beam} = 1.515$ GeV and a 1500 A torus field, and the other is with $E_{beam} = 4.462$ GeV and a 2250 A torus field. In both cases, the hardware trigger was intended to identify electrons, however, there was a substantial number of events that were triggered by non-electrons, particularly at the higher energies. Note that we did not use our knowledge of the beam energy for any of the event selection described below.

To perform time-based tracking, we normally use electron hits to calculate a candidate event start time (electron software trigger). However, for this analysis, we first identify the proton candidate hit via dE/dx in the time-of-flight (TOF) scintillator counters, we assume that the track for this hit has the proton mass, and then calculate a candidate event start time (proton software trigger). The top panel in Fig. 12 shows the W distributions for 4.462 GeV data after we select events for one proton and one electron. The solid line represents the proton software trigger events and the dashed line represents the nominal electron software trigger. Any contamination will be further eliminated via elastic kinematic constraints, as shown below. The bottom plot in Fig. 12 shows that event selections with one proton and one electron in opposite sectors substantially reduce inelastic events without losing elastic events.

Once events with one proton and one electron in opposite sectors are identified, we can substantially eliminate inelastic events by applying the co-planarity cut as shown in Fig. 13. The top figure shows the difference between ϕ_e and ϕ_p for $E_{beam} = 4.462$ GeV and the bottom figure is for $E_{beam} = 1.515$ GeV. The selection of elastic ep candidates are based on the cut,

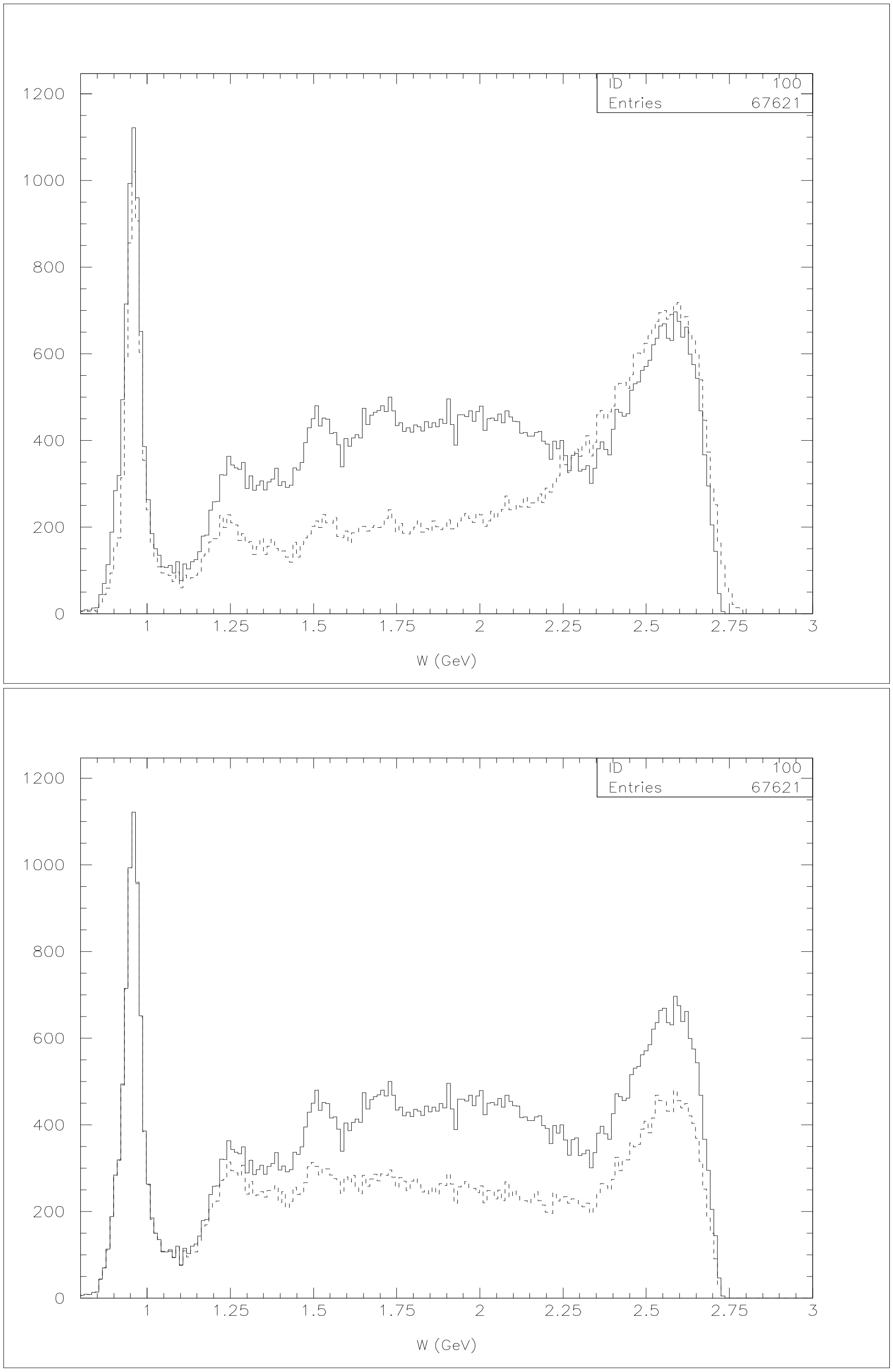

FIG. 12: W spectrum from E1C data for $E_{beam} = 4.462$ GeV after single-electron and single-proton events are selected. Top figure: Events triggered by an electron-software trigger (dashed) and or a proton-software trigger (solid). Bottom figure: Events with a proton trigger (solid) and combined with an electron in the opposite sector (dashed).

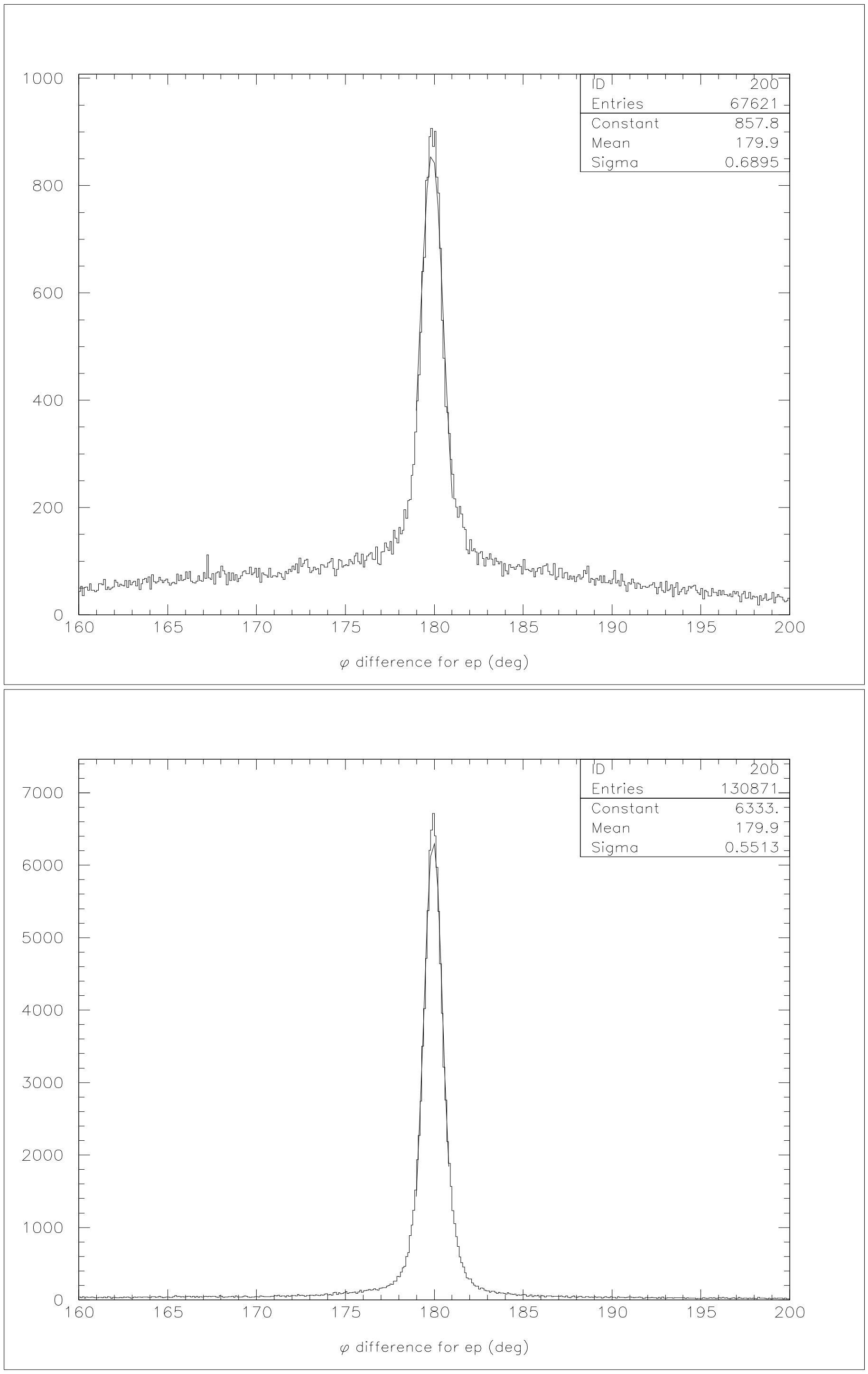

FIG. 13: ϕ difference spectrum between protons and electrons to select coplanar events. The top figure is from E1C data for $E_{beam} = 4.462$ GeV and the bottom figure is from $E_{beam} = 1.515$ GeV.

$178^o < \Delta\phi < 182^o$ for this analysis.

We then analyzed the data using two different methods. In method one, we used the measured scattered electron angle, θ_e, and momentum, p_e, to calculate the incident electron energy and scattered proton momentum and angle. In the other method, we used the electron and proton scattering angles, θ_e and θ_p, to calculate the other kinematic quantities. Please note that

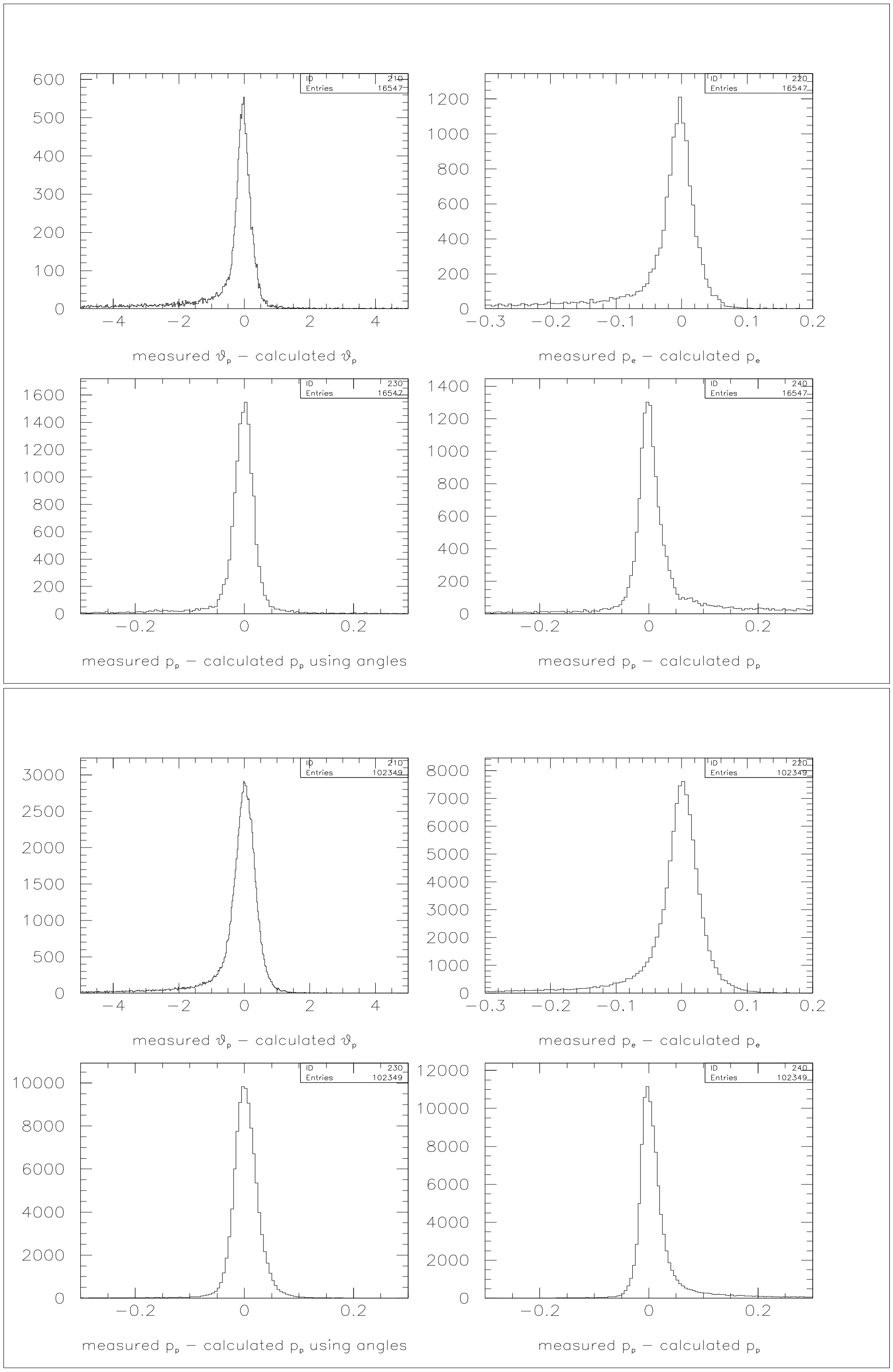

FIG. 14: Kinematic cuts using *ep* elastic kinematics after coplanar events are selected. Top left: difference between measured proton angle and calculated proton angle. The proton angle is calculated using the measured electron angle and momentum. Top right: the electron momentum is calculated using the measured electron and proton scattering angles. Bottom left: the proton momentum is calculated using the measured electron and proton scattering angles. Bottom right: the proton momentum is calculated using the measured electron angle and momentum. Top figure is from E1C data for $E_{beam} = 4.462$ GeV and the bottom figure is from $E_{beam} = 1.515$ GeV.

we did not use our knowledge of the incident electron energy for either method. Fig. 14 shows the difference between the measured and calculated kinematic quantities for both methods. The top panel is for $E_{beam} = 4.462$ GeV and the bottom panel is for $E_{beam} = 1.515$ runs.

Fig. 15 shows the W spectrum before (solid line) and after (dashed line) the kinematic cuts to eliminate inelastic events. The top figure is for $E_{beam} = 4.462$ GeV and the bottom figure is for $E_{beam} = 1.515$ GeV. (Note that we used our knowledge of the incident energy to compute W, but not to select the events plotted.) The long tail extending to large W and the peak at $W \approx 2.5$ are consistent with the radiative tail (ie: the electron radiates a photon before scattering) and would not be removed by these cuts.

This shows that we can isolate elastic scattering events in actual CLAS data even without knowledge of the incident electron beam energy.

2. Reconstruction of Monte Carlo simulation

To understand resolution and acceptance issues, we performed a Monte Carlo simulation. We used the program *ELAST_GEN* that produces radiated elastic events, and then we used the CLAS Monte Carlo simulation program (GSIM) for a complete model of the CLAS detector system, combined with the GSIM POST PROCESSOR (GPP) to introduce realistic resolution effects. We reconstruct the simulated events using the reconstruction program (RECSIS) that is used to reconstruct experimental data. This simulation and reconstruction package has been successfully used in almost all CLAS publications.

Fig. 16 shows comparisons of data with Monte Carlo simulation using kinematic cuts that select ep elastic events. These are for $E_{beam} = 1.515$ GeV. They clearly show good agreement between the data and the simulation.

We have also studied the acceptance and resolution effects between e^-p and e^+p radiated elastic events. Once we generate e^-p elastic events for $E_{beam} = 1.515$ GeV using the program *ELAST_GEN*, we replace e^- by e^+ to create e^+p radiated elastic events. By doing so, we can make sure that both events have the same kinematics for leptons and protons. We perform the same procedure to reconstruct both event files as described above using two different torus magnetic fields. One field is 1500 A and the other is 750 A.

Fig. 17 shows momentum and angular distributions for leptons (top) and protons (bottom). The solid line is for e^+p radiated elastic events and the dashed line is for e^-p radiated elastic events. In each figure, the top row is for a 1500 A torus field and the bottom row is for a 750 A torus field. The e^+ and e^- acceptances are quite different for $\theta < 25^o$ since out-bending events are bent to regions of larger acceptance. To avoid large systematic errors, we will limit the data to $\theta_e > 25^o$, which will affect only one ε bin at ε=0.9.

Fig. 18 shows a comparison of resolutions between simulated radiated e^-p and e^+p elastic events. The top figure is for a 1500 A torus field and the bottom figure is for a 750 A torus field. The solid line is for e^+p elastic events and the dashed line is for e^-p elastic events. The resolution from e^-p elastic is slightly better than e^+p elastic. This is mainly due to different values of $\int \vec{B} \cdot d\vec{l}$ for the two trajectories. This effect can be fully studied by reversing the polarity of the torus field in simulation and experiment to minimize the systematic errors.

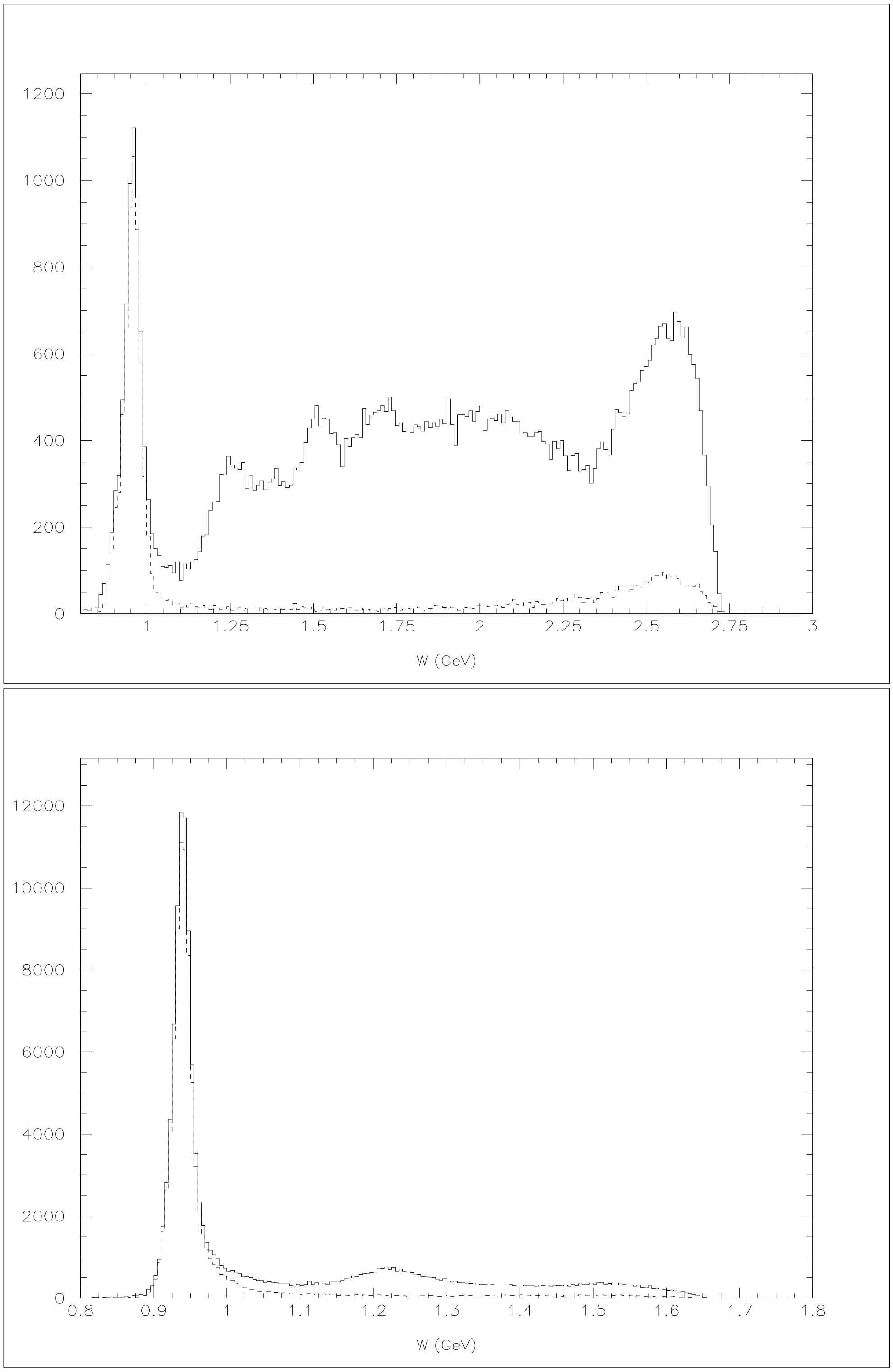

FIG. 15: W spectrum from E1C data after one-electron and one-proton events from the proton software trigger. The dashed lines represent ep elastic events after kinematic cuts were applied. The top figure is from E1C data for $E_{beam} = 4.462$ GeV and the bottom figure is for $E_{beam} = 1.515$ GeV.

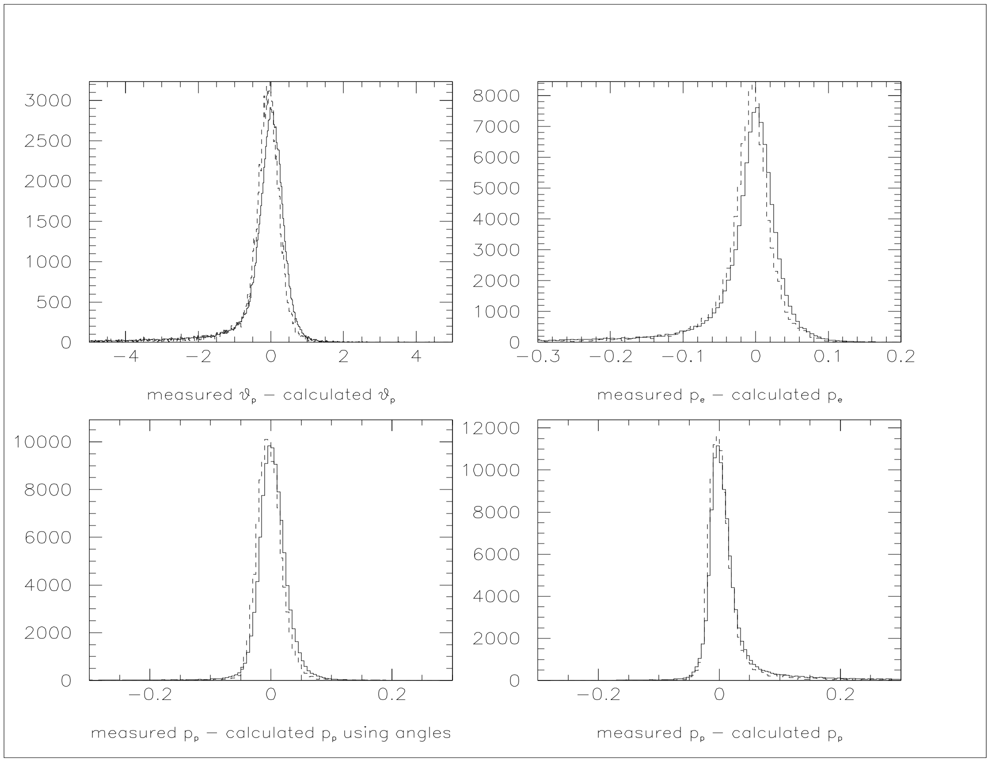

FIG. 16: A comparison of kinematic cuts between data and Monte Carlo simulation for $E_{beam} = 1.515$ GeV. The solid line is for data and the dashed line is for simulation.

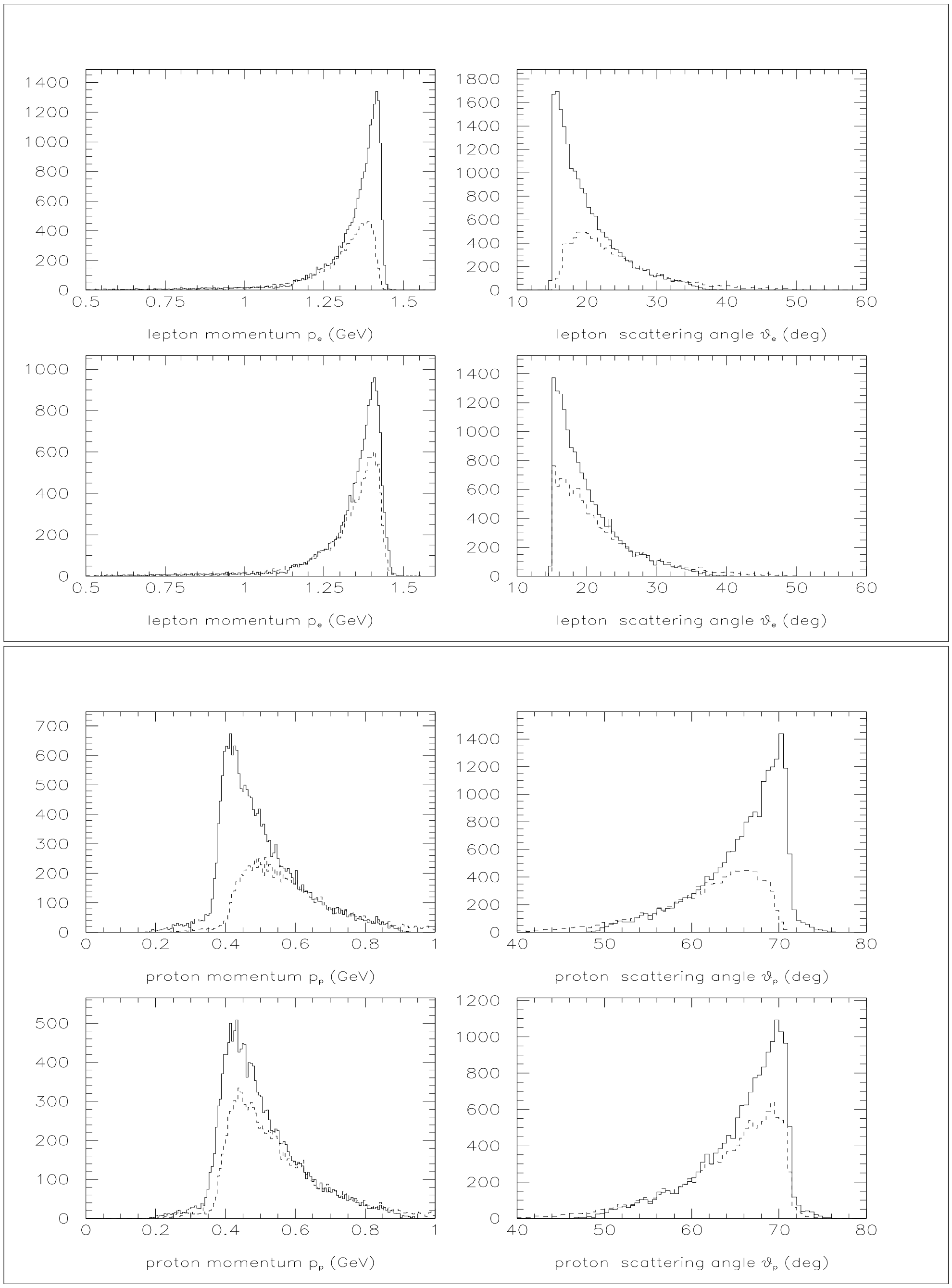

FIG. 17: A comparison of momentum and angular distributions from simulations for radiated e^-p and e^+p elastic events reconstructed using different CLAS torus fields. The solid line is for radiated e^+p elastic, and the dashed line is for radiated e^-p elastic. The top panel is for lepton kinematics and the bottom panel is for proton kinematics. In each figure, the top row is for a 1500 A torus field and the bottom row is for a 750 A torus field.

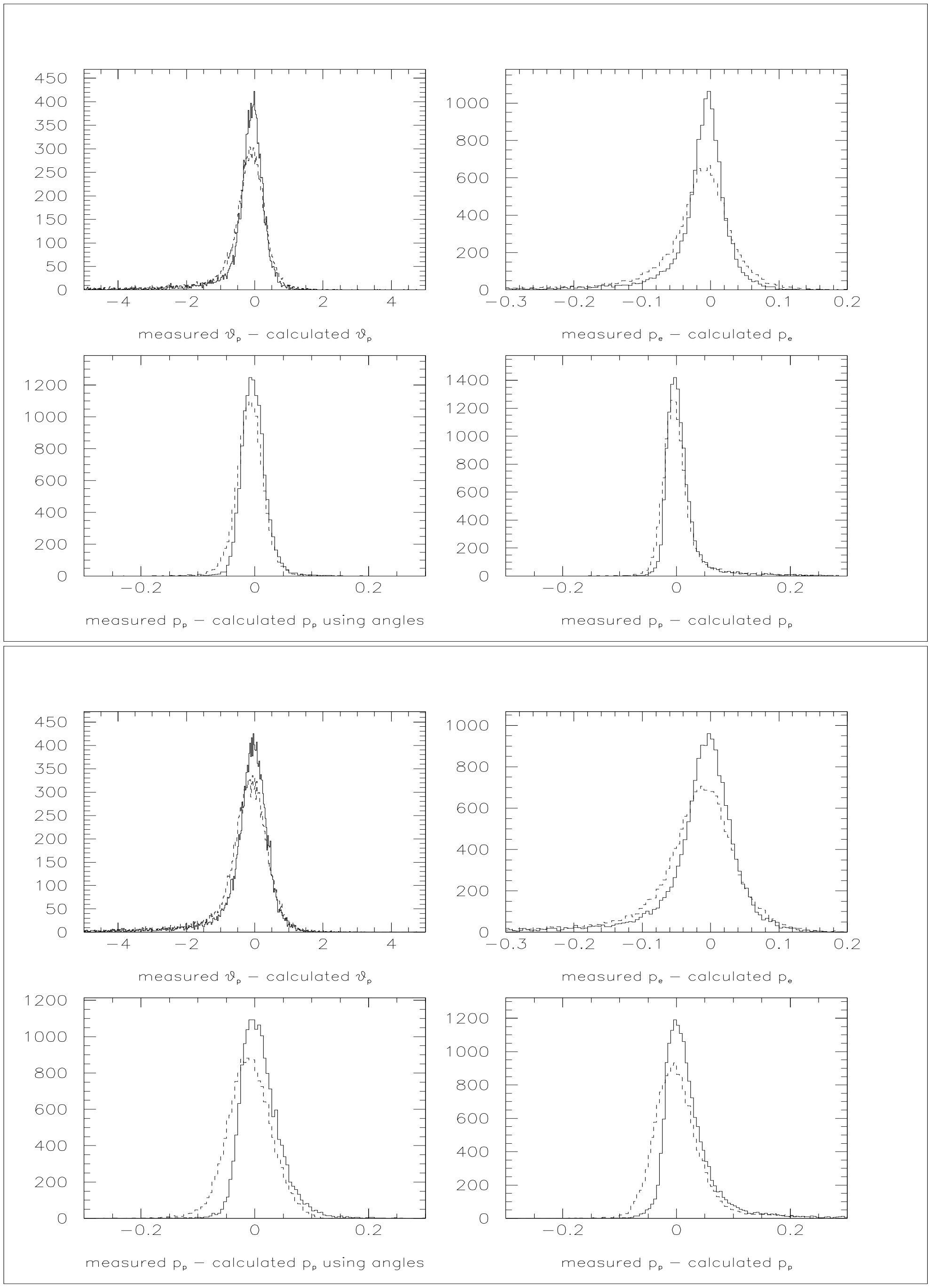

FIG. 18: A comparison of resolutions between simulated radiated e^-p and e^+p elastic events. The top figure is for 1500 A and the bottom figure is for 750 A. The solid line is for e^+p elastic events and the dashed line is for e^-p elastic events

F. Backgrounds

The prospect of creating secondary beams always raises issues of backgrounds and beam quality. The technique proposed here for producing the lepton beam is relatively clean, partly because the experiment can be successfully performed with a small beam current, taking advantage of the large acceptance of CLAS. Nonetheless, because of the spectrometer's innately 'open' design, it is quite vulnerable to background generated anywhere upstream, and so a thorough study is required.

There are several major categories of backgrounds to consider:

1. electromagnetic background generated from the photon collimator and from the new beamline devices: photon blocker, low-energy collimators, and the magnet yokes.

2. hadronic background from the photon blocker.

3. background from the tagger vacuum box and beam dump

4. Møller and Bhabha electrons produced in the hydrogen target.

These will be discussed in detail in the following sections.

Three different simulations have been employed for these studies, all based on GEANT. The first is a simulation of the beamline components that is based on GEANT 3.21. It will be referred to as the 'beamline simulation'. It contains the following elements: tagger magnetic field, sweeping magnet magnetic field, four dipole magnet magnetic fields; radiator material, converter material, four dipole magnet yokes, photon blocker, low-energy collimators, lead shield wall, shielding snout. No fringe fields were included. Drawings of these components can be seen in Figures 5, 6, and 7.

The second simulation was performed by using a GEANT 4 implementation [29],[30] referred to as the GDINR simulation[32]. It includes the radiator, photon collimator, converter, and the tungsten blocker, with no magnetic fields. This code is especially accurate for photoproducing hadrons. Because there are no magnetic fields, this simulation collides the produced lepton beam with the blocker, unlike the real situation; however, it is only a small error since the converter is quite thin. Thus it will give a slight overestimate of the background rates.

The third simulation is the standard CLAS simulation, referred to as GSIM [31]. It includes all components of CLAS and has been extensively tested and developed.

1. *Electromagnetic background from beamline components*

The electromagnetic background from the beamline components as a whole was estimated using the beamline simulation, and the emission specifically from the photon blocker was estimated using GDINR. Figures 19, 20, and 21 show rates related to photons, positrons, and electrons respectively, emitted from the photon blocker. In these plots the full angular range and momentum range are indicated, however, only a small part of this background makes it into CLAS due to the lead shielding wall between the two. Two sources of background can happen here: either the produced particles go through the small hole in the center of the shielding wall, or they have enough energy to create a shower that penetrates the shielding wall. An estimate of the first effect can be obtained by considering the solid angle subtended by the two-inch hole in the shielding wall for a point source at the center of the blocker. The distance between the two is 216 cm, thus the half angle is 0.68 degrees and the solid angle is 0.4 msr. From the lower plot of Fig. 19, using the right-hand axis, we derive a rate of 40 MHz for photons of 100 MeV or greater, assuming a 1 μA beam incident on the tagger. From Figures 20 and 21 the rates for positrons and electrons would also be expected to both be 40 MHz, however, these will both be deflected by the two dipoles following the photon blocker. The leptons from the blocker that successfully pass through the shield wall aperture will come from a larger angle range, where the rate is several orders of magnitude smaller. This effect is handled correctly by the beamline simulation, as are any particles that penetrate through the wall.

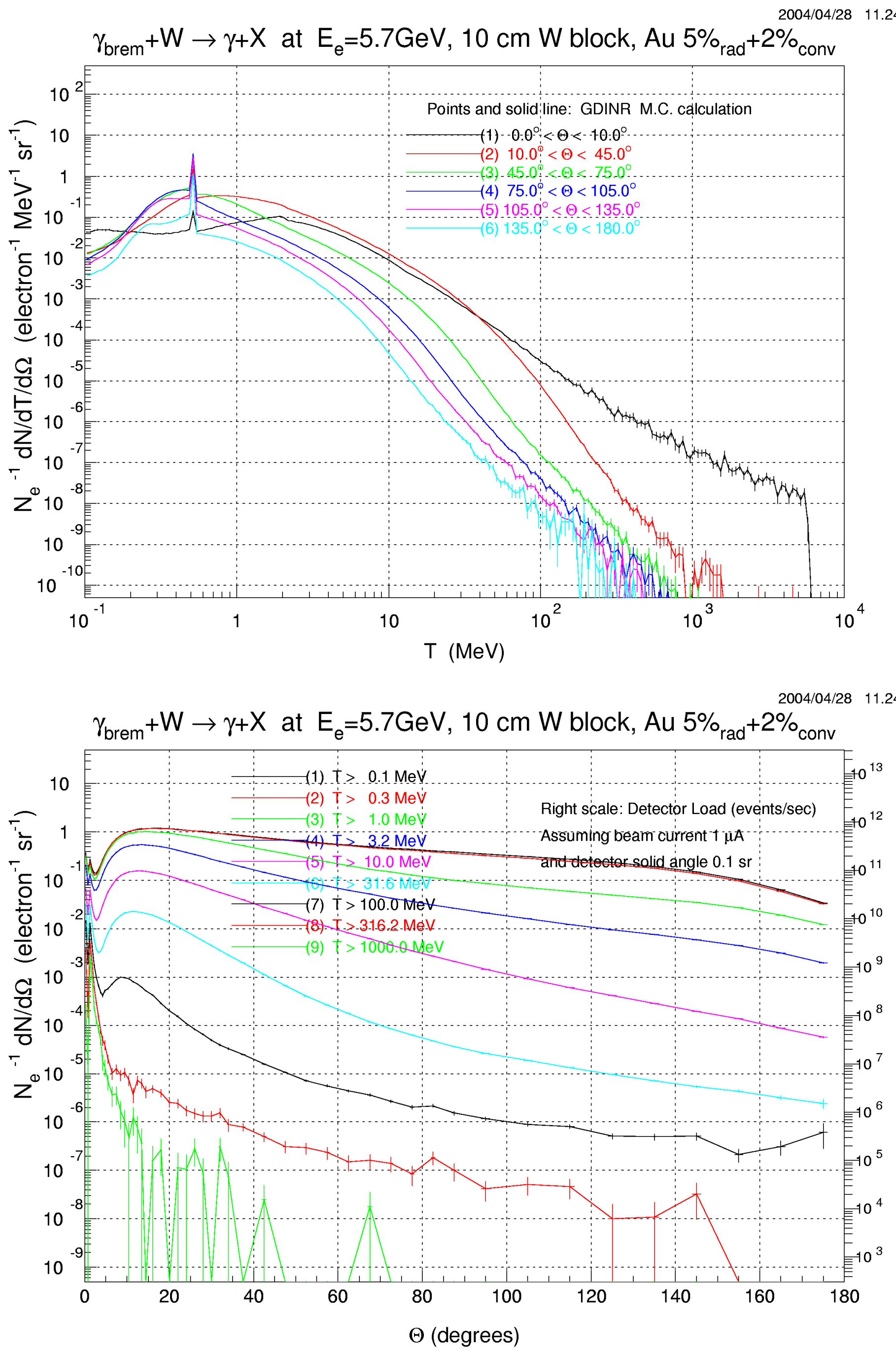

FIG. 19: Photon rates from the photon blocker according to the GDINR simulation.

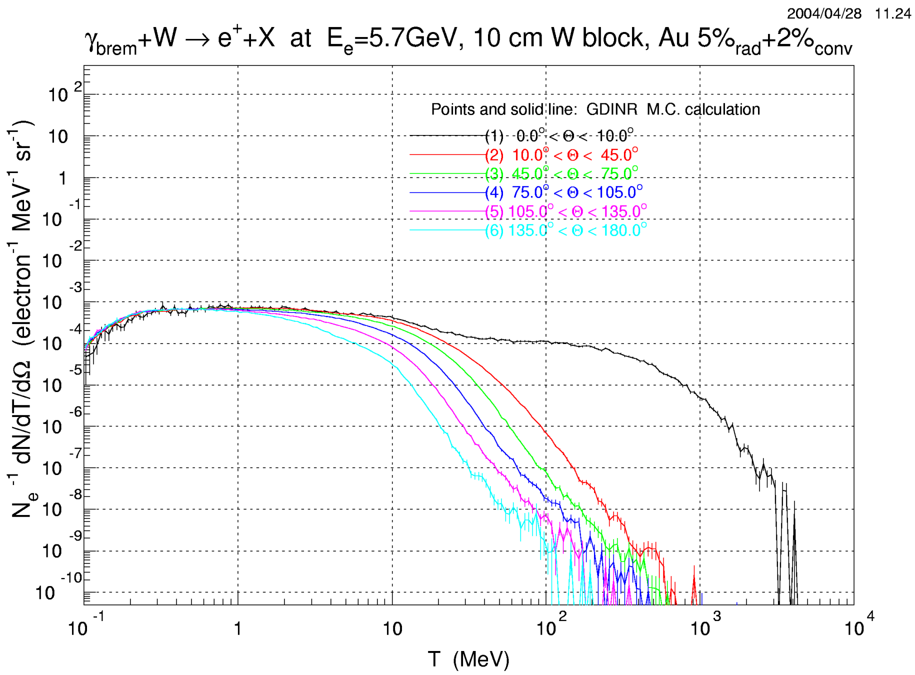

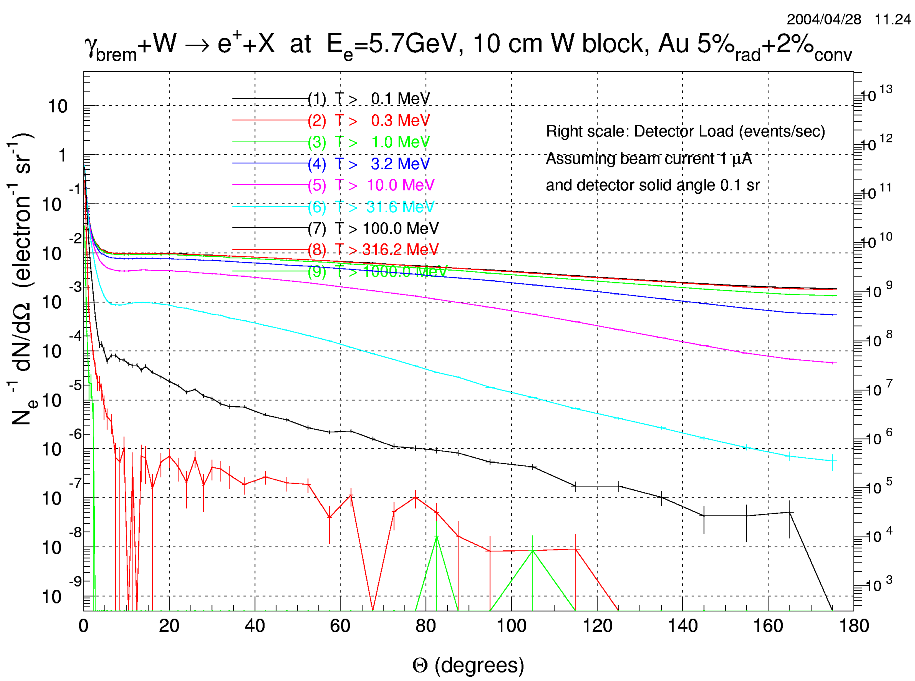

FIG. 20: Positron rates from the photon blocker according to the GDINR simulation.

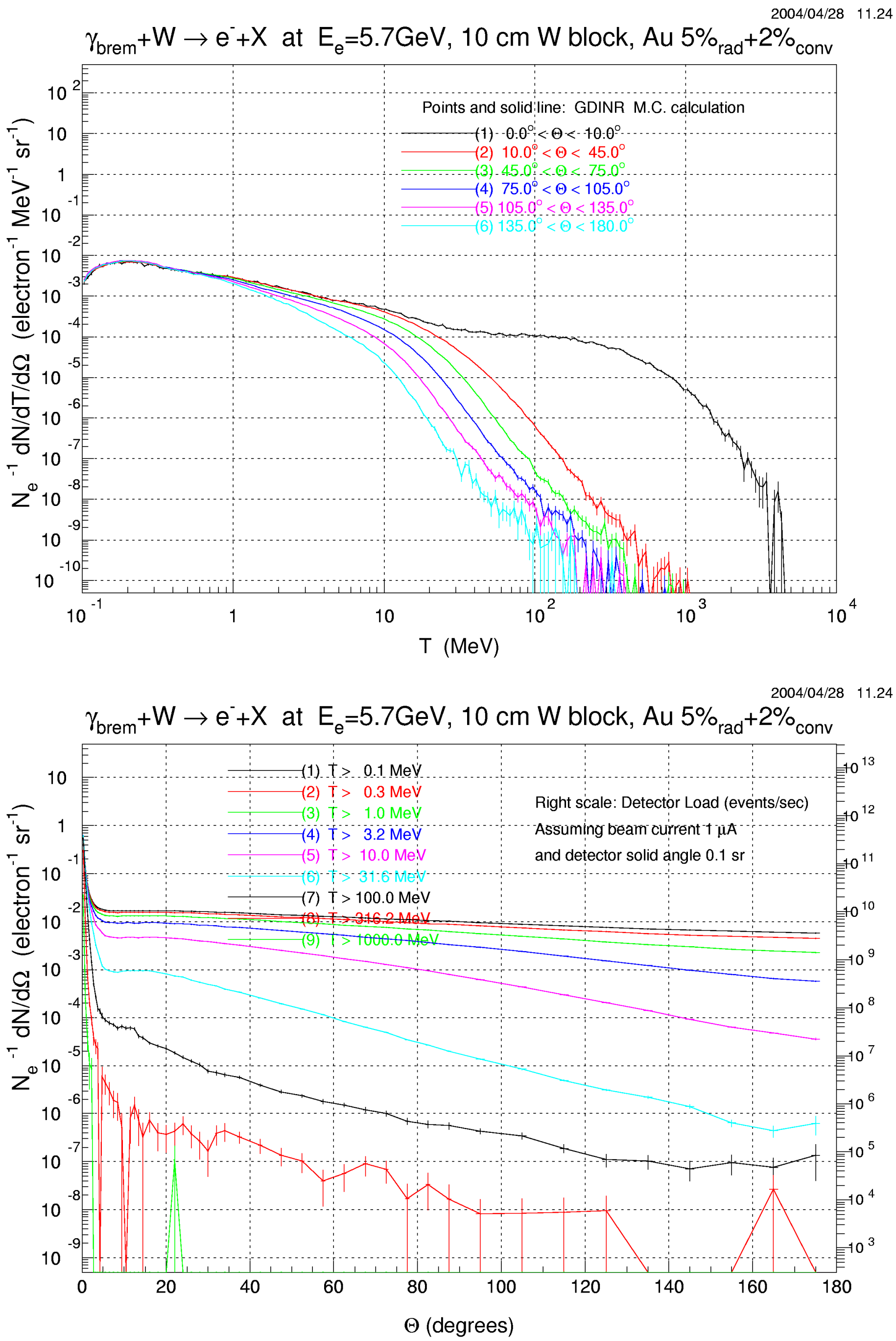

FIG. 21: Electron rates from the photon blocker according to the GDINR simulation.

The 40 MHz of photons will produce some background, however, because it is mostly low energy, the background will not resemble the elastic scattering events of interest. Since 10 MHz of high-energy tagged photons (and many untagged photons) typically produce very clean events in CLAS in routine photon beam running, it is not expected that accidentals from photons will be a problem.

A more interesting concern is that if there is any flux of leptons from the blocker, it will not be properly accounted for during flux measurements. It is planned to block one of the lepton types using the low-energy collimators while measuring the flux, however, any leptons that come from the photon blocker will not be stopped. The size of this effect can be accurately simulated, however, and also can be estimated experimentally by blocking both lepton types simultaneously. If the GDINR estimate is correct, however, the rate of such events is still 3-4 orders of magnitude less than that of the primary lepton beam, and therefore should be of little concern.

Turning now to results from the beamline simulation, in Fig. 22 is shown a representation of the charged track trajectory in the $x - z$ plane. The upper panel shows tracks of 300 MeV and greater, and the lower panel shows all tracks below 300 MeV. In the upper plot, the dark spot in the middle is the photon blocker, where photon showers create charged particles that are mostly contained within the blocker. The shield wall can be seen as a vertical line at $z = -700$ cm. Since the opening in the wall is 5 cm diameter, essentially all of the tracks above 300 MeV make it through the shield wall and proceed to the target location at z = 0 cm. The tracks that curve around the photon blocker are electrons and positrons produced in the converter and routed around the blocker by the chicane.

In the lower panel of Fig. 22, one can see that most of the low-energy leptons are shielded away by the shield wall and the magnet yokes, however, there are some low-energy tracks that pass through to the target region. The low-energy component that hits the target is of little concern, because the rate is low and the likelihood of producing an event that looks like a high-energy elastic scattering is small. However, the tracks at larger distance from the beamline could produce showers in massive support structures, or could directly produce hits in the Region I drift chambers. The rate of the events that actually hit Region I needs to be carefully quantified by a GSIM simulation; early estimates (see below) indicate that these contribute a few tracks in Region I per event, i.e. comparable to the Møller rate for normal CLAS electron beam running. The tradeoff between having enough low energy electrons to provide low-epsilon data, and having tolerable background rates, can be optimized experimentally by positioning the low-energy collimators, since the majority of the background tracks come from beam scraping on these collimators.

Another view of this issue is given in Fig. 23, where on the vertical axis is the lepton momentum, and on the horizontal axis is lepton distance from the beamline, at the target location (z = 0 cm). In this plot it is clear that the low-energy background arrives at larger distances from the beamline, mostly missing the target, and likely hitting the Region I drift chambers. The percentage of leptons at a radial distance from the beamline sufficient to hit Region I is approximately 4%; of these, perhaps half will actually enter the drift chamber, while the others will be stopped in the torus coil casing, since these tracks populate the forward angles where the acceptance is smallest. Estimating this background at 2% of the total flux yields approximately 25 MHz. If the effective time window of Region I is 200 ns, this predicts each event will on average have 5 accidental lepton tracks at low angles. These tracks will, in general, not point toward the target, but rather will point upstream.

A more extensive analysis of the origin of these tracks is likely to reveal methods for getting rid of most of them, such as extending the carbon portion of the shielding snout out further. Such a study would be undertaken before the final design of the beamline. Even with the

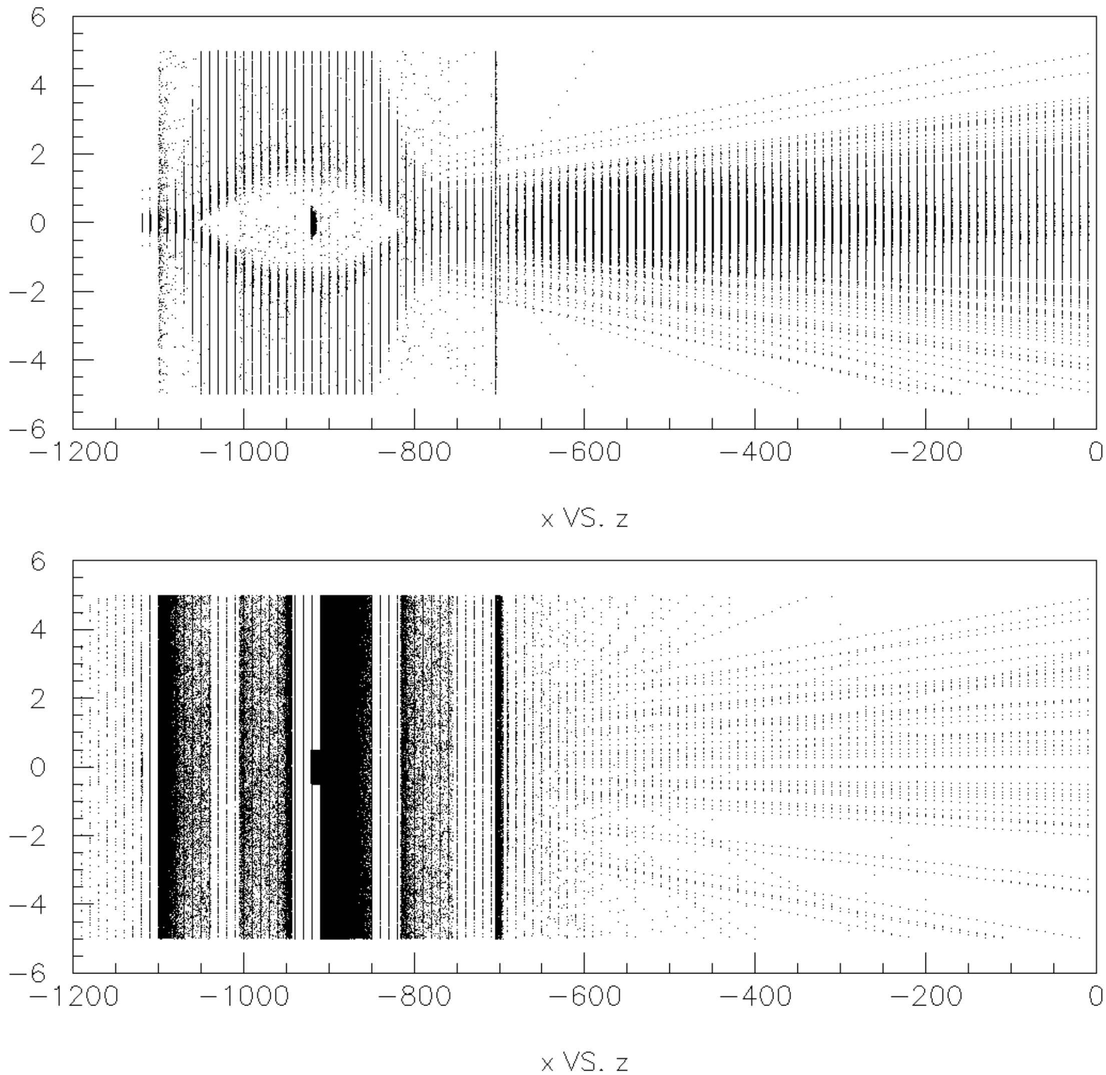

FIG. 22: An illustration from the beamline simulation of charged particle trajectories through the chicane and shielding system. The upper plot indicates tracks with energy greater than 300 MeV, while the lower plot indicates tracks with energy less than 300 MeV. The location of the photon blocker can be seen at −930 cm, while the lead shield wall is at −700 cm.

elementary design discussed here, this background rate is tolerable.

2. Hadronic background from the photon blocker

The hadronic rate from the photon blocker has been estimated using GDINR. While there will also be hadronic production from the nickel photon collimator and the low-energy collimators, the dominant rate that affects CLAS must be from the photon blocker, since it absorbs the full high-energy photon flux and it is only a few meters from the CLAS center. Figures 24, 25, 26, and 27 show the rates corresponding to π^+, π^-, neutrons, and protons respectively.

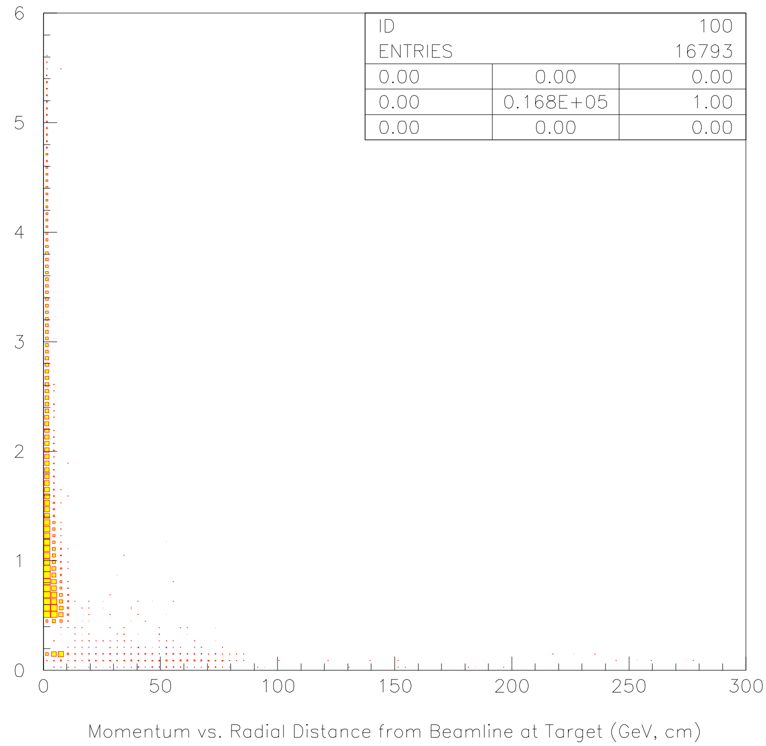

FIG. 23: A plot from the beamline simulation of the momentum of leptons in GeV (vertical axis) vs. the radial distance from the beamline in cm (horizontal axis). The plot is made for z = 0 cm, i.e., at the target location. The gap in momenta between 0.2 and 0.5 GeV is created by the photon blocker. Background events can be seen at low momenta and larger distance.

Inspecting these, it is useful to pick out a few representative numbers for estimates. An average value from the right-hand axis of the bottom plots is 10^6 Hz for pions, 10^7 for neutrons, and 10^6 for protons. These numbers partially take into consideration that the charged particles will lose energy in passing through the lead shielding wall as well as a significant length of the tungsten photon blocker and perhaps also iron magnet yokes. If these are scaled by π steradians, the resulting rates are 30 MHz for pions and protons, and 300 MHz for neutrons, spread out over the full volume of CLAS. The lower-energy component of the charged particles will not penetrate Region II because of the torus field, and any tracks going in the other regions will not point at the target.

Although these rates are significant, they do not take into account the shielding effect of hadronic interactions in the magnet yokes nor the shield wall. Further studies are required to determine if additional shielding is necessary to reduce the charged hadron rates.

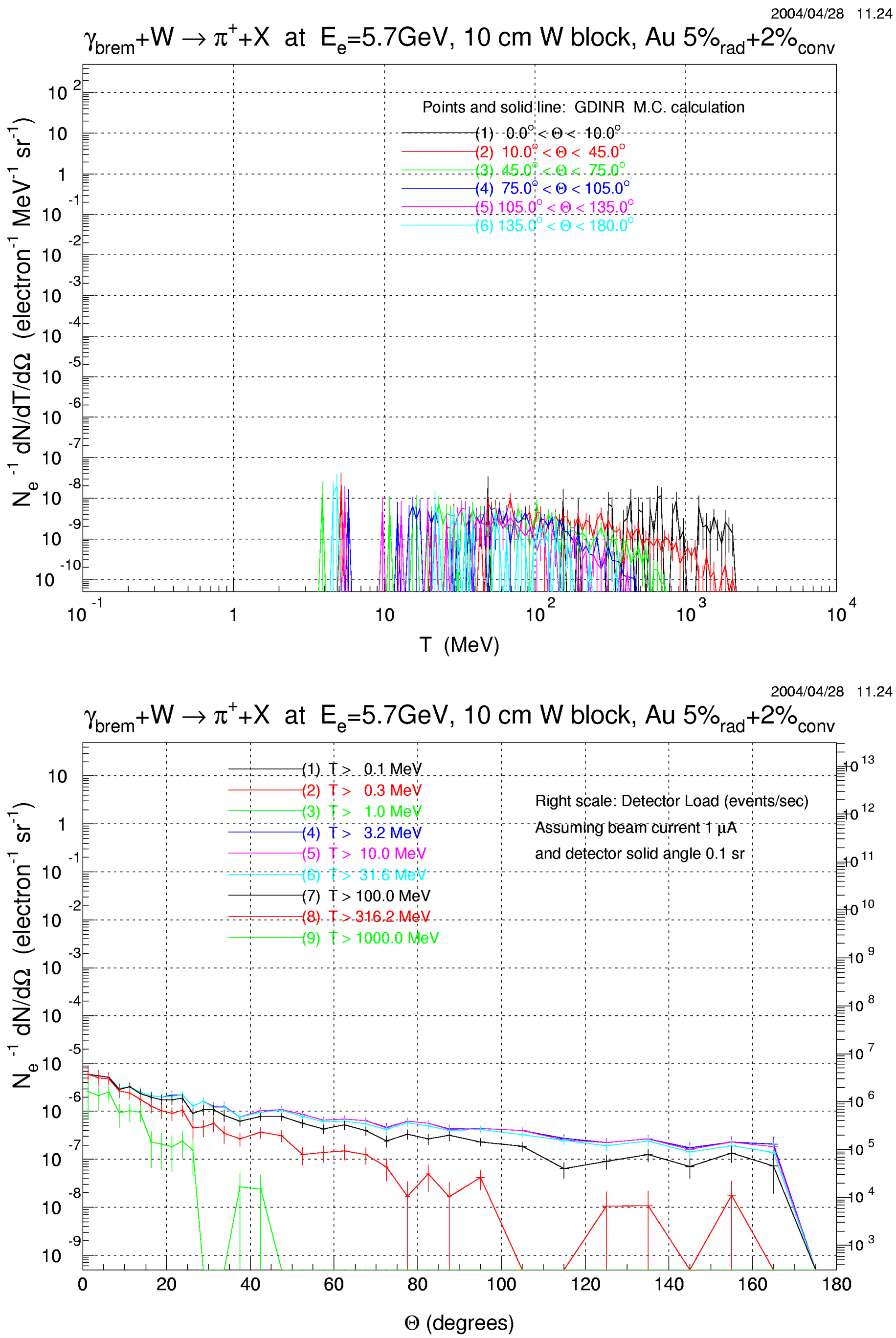

FIG. 24: Positive pion rates from the photon blocker according to the GDINR simulation.

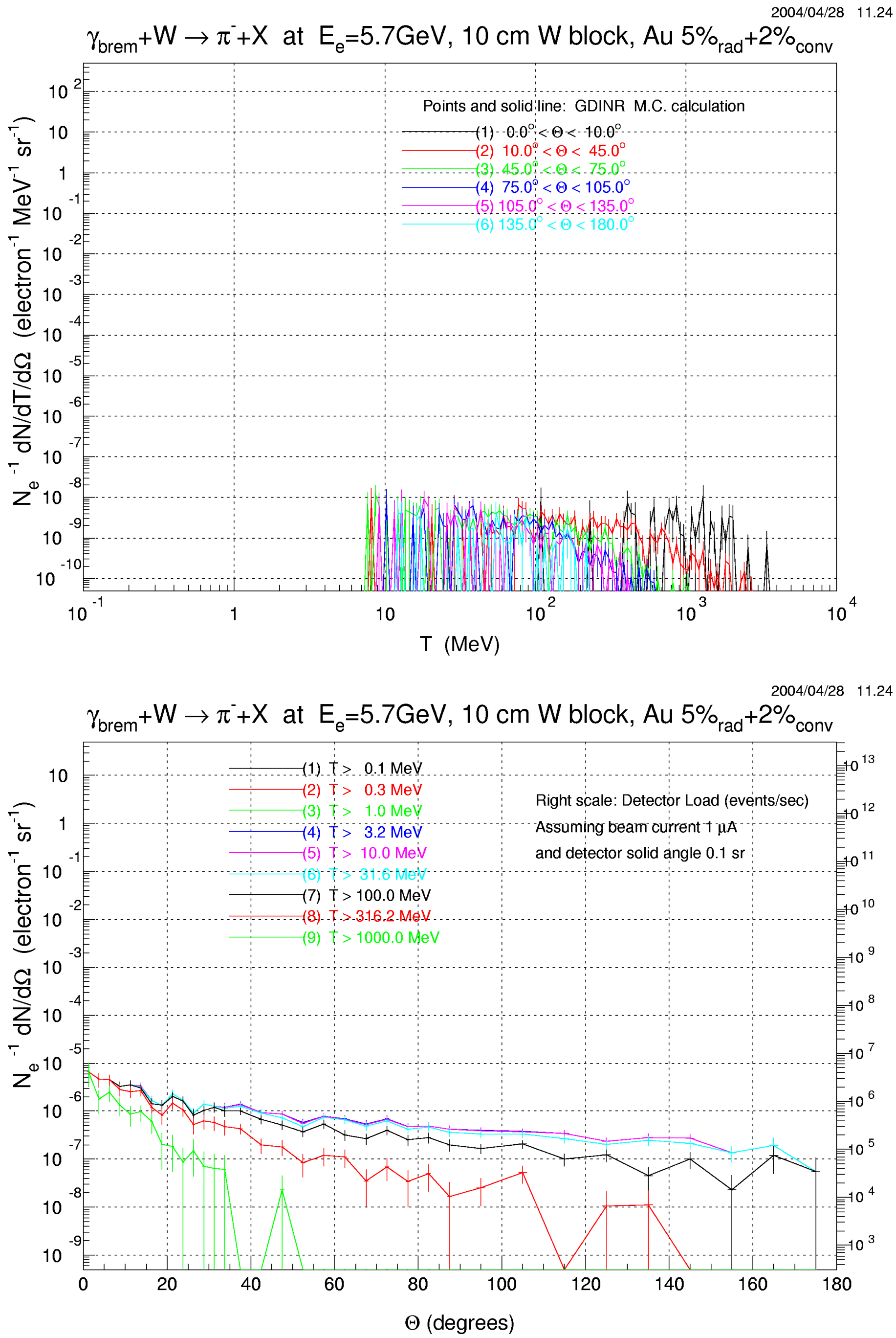

FIG. 25: Negative pion rates from the photon blocker according to the GDINR simulation.

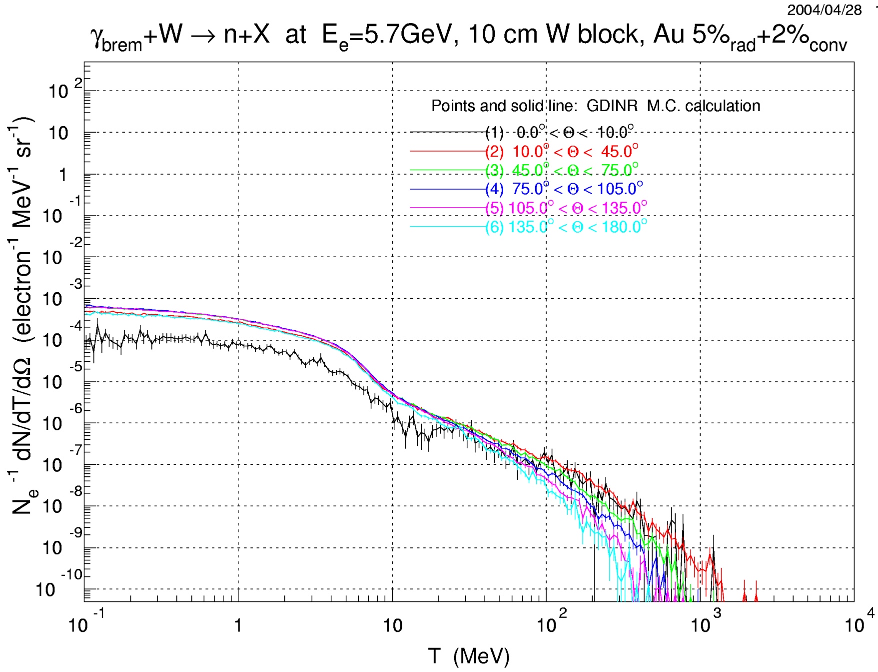

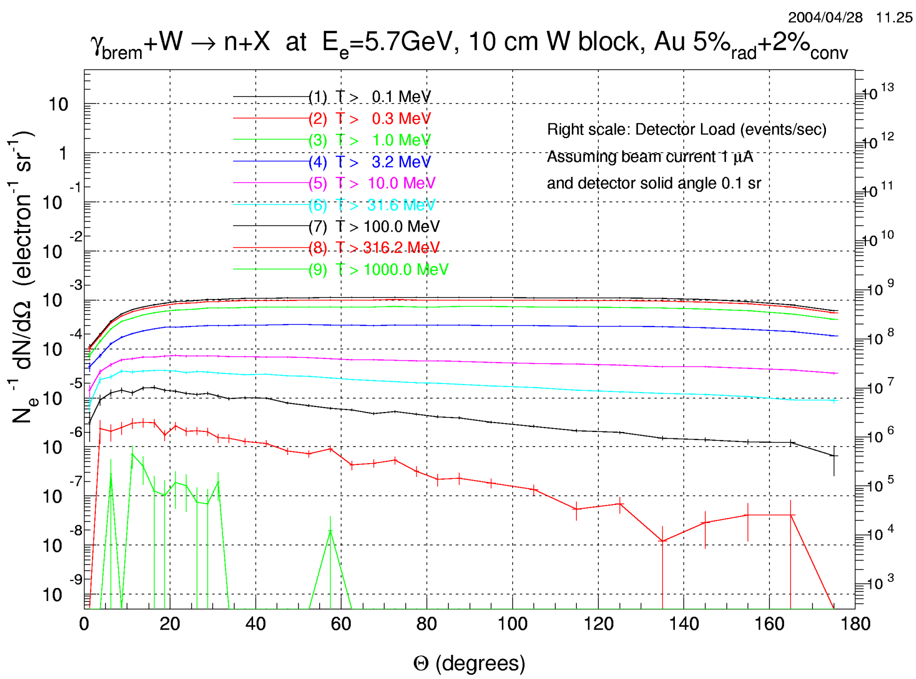

FIG. 26: Neutron rates from the photon blocker according to the GDINR simulation.

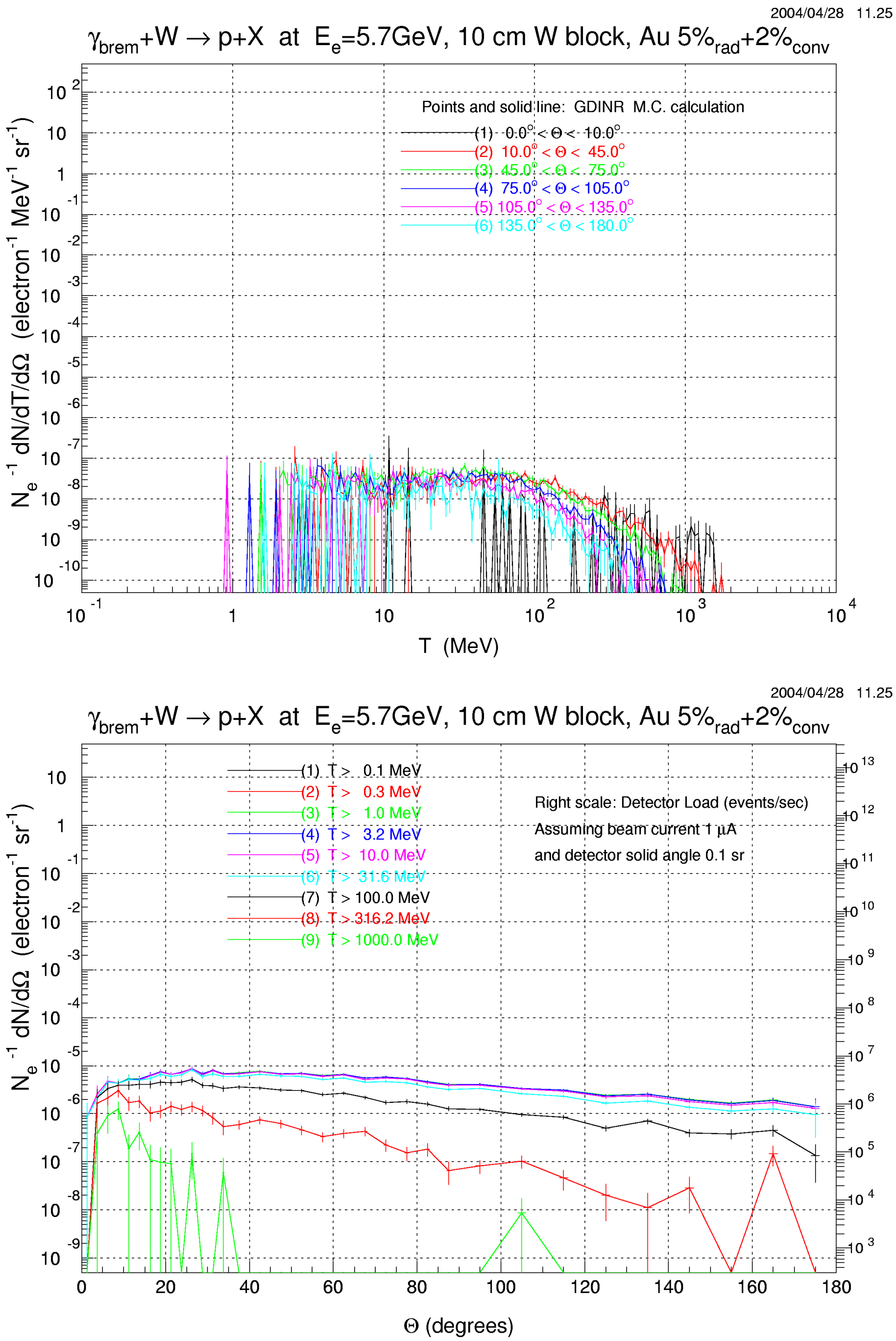

FIG. 27: Proton rates from the photon blocker according to the GDINR simulation.

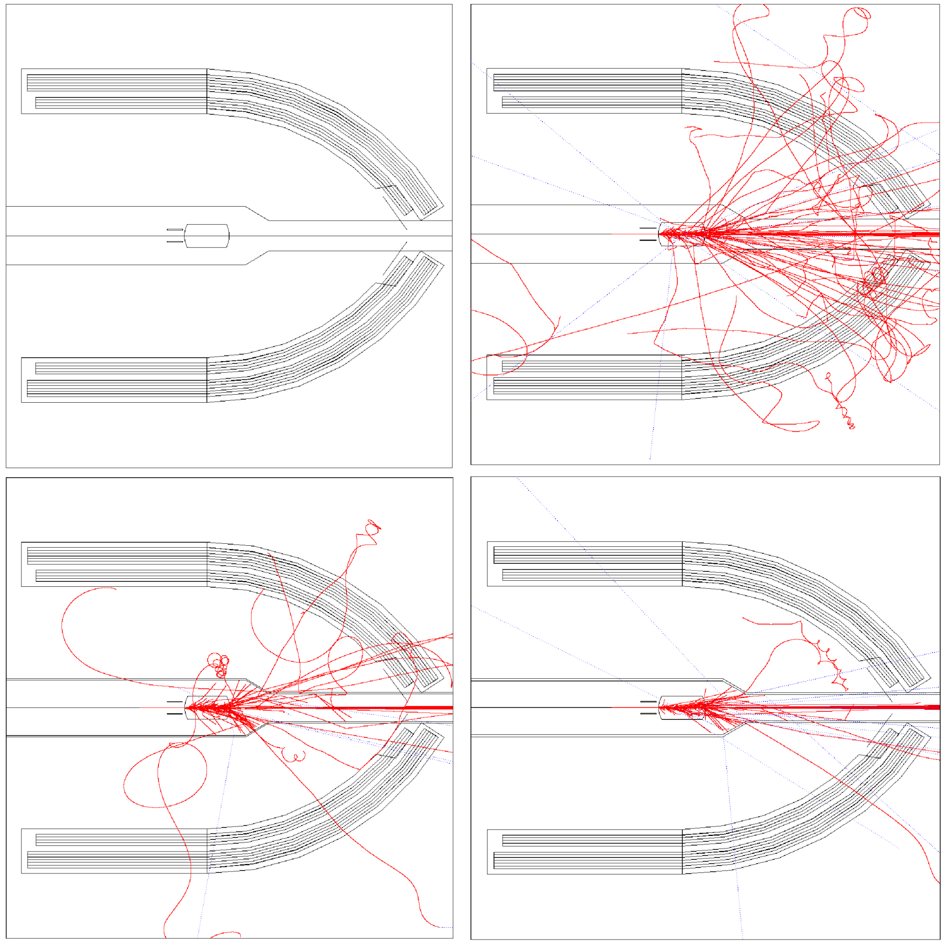

FIG. 28: A GSIM simulation of the effect of passive shielding on Møller and Bhabha scattered electrons. The upper left panel shows the geometry of the simulation near the beamline; a cryotarget in the center is surrounded by a beam pipe, and the Region 1 drift chamber can be seen. In the other three panels, the accidental background due to 250 pA of electrons and positrons in a 200 ns window is shown. The upper right-hand panel has no shielding except for the liquid hydrogen itself; the lower left panel has a 6 mm thick carbon beam pipe; and the lower right panel has a 10 mm thick carbon beam pipe. The subsequent reduction in background is visible. The actual implementation would not put the extra material close to the target, but rather, next to the drift chamber, to minimize the degradation of the angular resolution.

3. Tagger-related background

Simulations are not available for tagger-related background, but there is extensive running experience. The two possible sources of background are scattering from the vacuum flange at the beam exit of the tagger vacuum box, and leakage out of the tagger dump up into CLAS. With the existing shielding and currents of up to 130 nA, neither of these have been a problem. With an order of magnitude more tagger current, these backgrounds may become visible, although since they are currently negligible, this is unlikely to become a serious problem. The ideal approach is to do a brief test run at the end of a photon beam run, and increase the current to see if there is a visible effect in the data.

4. Møller/Bhabha electrons

It is currently envisioned that 1 μA of beam current on the tagger will produce 250 pA of total current on the hydrogen target. This corresponds to a luminosity of $1.3 \times 10^{33} cm^-2s^-1$. This is higher than CLAS can normally run without using the minitorus. Use of the existing minitorus is not optimal, because the downstream aperture through the magnet is smaller than the lepton beam that needs to pass through it. Two clear possibilities exist for managing this background: construct a new minitorus, or add passive shielding in front of the Region 1 drift chamber.

If necessary, a new minitorus can be constructed that has a larger downstream aperture; operational experience with 'straight-track' runs taken for aligning drift chambers indicate that only one-third of the standard mini-torus field would be needed to run this experiment[33]. Therefore, the perturbation on the charged particle tracks would be quite small. While in principle there will be outgoing positrons from Bhabha scattering which will be anti-shielded by a minitorus, the rate of these is greatly suppressed relative to scattered electrons.

In this experiment, the larger target thickness itself will suppress the lowest energy Møller/Bhabha electrons, in addition to the scattering chamber. Additional thin mechanical shielding can be mounted to reduce this lowest-momentum component further, without serious impact to the angular resolution. A combination of measures such as these is likely to be adequate to allow operation without the minitorus magnet. An example of this is shown in Fig. 28, where 6–10 mm of carbon passive shielding is shown to significantly reduce this background. This material would be installed close to the chamber, to reduce the degradation of angular resolution. As a reference, 6 mm of carbon is less than the amount of material charged particles encounter when passing through the CLAS drift chambers. Since most of the soft particles go in the forward direction, it may be preferable to omit the shielding in the backward direction, so that the backward-scattered particles of interest will not be affected.

It is not yet clear which of these two alternatives is preferable; however, both are feasible.

G. Systematic errors

The purpose of the experiment is to precisely compare the e^+p differential cross section to the e^-p differential cross section. Here is a list of the potential sources of systematic error:

1. differences in the positron and electron incident flux
    - differential electron-positron attenuation in matter
    - differences between low-flux and high-flux beams
    - differential trajectories through the magnetic system
        - imperfections in one pole face
        - changes in angle/position of the incident photon beam
        - reproducibility of magnetic field when switching dipole magnet polarities
        - magnetization of local objects
        - Earth's magnetic field

2. differences in the acceptance of the protons from the two reactions

3. differences in the determination of the electron and positron momentum vector

4. differences in the acceptance of the electrons and positrons
   - CLAS geometrical acceptance differences
   - differential e^+/e^- attenuation (can also be caused by path length differences)
   - CLAS detector inefficiencies, errors and miscalibrations
   - differential phi-focusing for trajectories near the torus coils

5. contamination by background process
   - inelastic lepton-proton scattering: $e^{\pm}p \to e^{\pm}p\pi$
   - virtual bremsstrahlung in the target: $\gamma p \to p\pi X$
   - virtual bremsstrahlung in the target walls: $\gamma n \to p\pi^-$

We will use several powerful techniques to reduce the effects of the systematic errors:

1. measure the flux of both incident beams, both destructively at the target and non-destructively where the beams are dispersed

2. use the same target for both beams

3. reverse the magnetic field in the separator magnet chicane, interchanging the paths of the two lepton beams

4. trigger on any two charged particles in opposite sectors (to avoid hardware electron/positron identification biases)

5. determine the scattering kinematics using only the proton information (independent of beam charge) and use the lepton only to determine that the event is elastic

6. use a low CLAS torus magnetic field

7. reverse the torus magnetic field, interchanging the scattered electron and positron trajectories

8. compare asymmetries measured in different CLAS sectors

9. reduce endcap contamination by cuts and by empty target subtraction

10. use the CLAS EC and Cerenkov counters to measure the pion contamination at forward angles

To first order, the electron and positron beam fluxes should be completely identical. The two beams are created simultaneously by pair production in a photon converter. The only differences in the two beams could come from a) differential beam attenuation in the finite thickness of the converter, b) differences in beam transport from the converter to the target, and c) differential beam attenuation in the 20-cm long target. According to the PDG, at lepton energies above 500 MeV, attenuation of positrons and electrons is completely dominated by bremsstrahlung (which is identical for both particles). Positron annihilation and Bhabha (e^+)

and Moller (e^-) scattering are all negligible. With a 2% converter, only 1% of the converted leptons will be lost to bremsstrahlung in the converter. Since the difference between electron and positron attenuation in materials is much less than 10%, the beam flux asymmetry from the converter is much less than 0.1%. Similarly, the 20 cm LH_2 target is about 3% of a radiation length so differential attenuation in the target is less than 0.1%. Therefore differences in beam flux should only come from differences in beam transport. We will deal with these possible differences in two ways.

We will significantly reduce any effects from asymmetric beam transport by reversing the magnetic fields in the separator magnet chicane. This will interchange the incident electron and positron beams. We will carefully cycle the chicane magnets to minimize the effects of hysteresis. To the extent that the field values are reproducible, and that there are no other magnetic fields affecting their trajectories, the electrons and positrons will follow exactly the same path when the separator field is reversed. Averaging the data taken with the two separator field polarities will average out any differences in the beam transport through the chicane and any differences in the flux monitoring detectors.

There will be some unavoidable difference in the magnetic fields of the two chicane polarities due to magnetization of nearby materials, unreproducibility of the magnetic field, and the Earth's magnetic field. This difference will have two possible effects. The first would be to change the amount of flux reaching the target and the second would be to change its position on the target.

We expect that the difference in $\int B \cdot dl$ between the path followed by electrons and that followed by protons with reversed chicane field (and vice versa) will differ by at most 1%. Since all of the beam, except that part cut off by the low-energy collimators, is transported to the target, a small change in the magnetic transport will only affect the value of the low-energy cutoff. Since the software threshold on the incident particle energy will be larger than the collimator-cutoff, a small shift in the collimator cutoff will not affect the incident flux.

Non-reproducibility and non-reversibility of the chicane magnetic fields will change the beam position on target by about 1 mm. The maximum beam deflection for low energy ($E = 0.5$ GeV) leptons in the chicane is 10 cm. A 1% difference in $\int B \cdot dl$ would then shift the path of the low energy leptons by 1 mm. We will measure the position and energy distribution of each lepton beam after each field reversal in the chicane to an average of better than 1 mm.

Since over 99% of the incident leptons will hit the 10-cm diameter target and since the lepton distribution is strongly peaked at the center of the target, a 1 mm shift in the beam centroid will change the low energy part of the beam that hits the target by less than 0.1%. The offset of higher energy leptons would be significantly smaller as it is proportional to $1/E$.

The variation of beam position on target will affect the average target length. The 20-cm long, 10-cm diameter target will not be a perfect cylinder. The downstream target face will have a radius of curvature of probably 20 cm. This means that it will be 207 mm long in the center and 200 mm long at the edges. A 1-mm beam shift will change the average target thickness (for that energy lepton) by at most 0.2%. In addition, we will apply software cuts to remove the effects of the entrance and exit windows. This will also remove the effects of the downstream window bulge. If necessary, we can also use a pressurized gas capsule to force the upstream window to bulge in, cancelling the effects of the downstream bulge and making the target length constant.

The geometrical acceptance of CLAS is determined primarily by the torus cryostat. The cryostat is 1.5 m from the target. A 1 mm shift in beam location will thus decrease the solid angle in one sector by approximately 0.1% and increase it in the opposite sector by the same amount.

We will measure the centroids of each of the lepton beams as a function of incident lepton energy. We will easily be able to measure centroid locations to within 1 mm with the proposed flux monitoring system.

We will also directly measure the flux in the two beams for both chicane polarities. The flux measurement serves two purposes. It will measure whether the e^+ and e^- beams are identical and, if they are not identical, how much they differ as a function of energy and position. It will also measure the absolute energy distributions of the two beams.

The flux measurement techniques are described in detail in Sec III C. We will measure the flux of each beam immediately in front of the target as a function of energy and position on target using a position sensitive detector followed by an electromagnetic calorimeter. We will also measure the flux of the unused low-energy part of each beam immediately before the second chicane magnet where the beams are separated and dispersed.

We will make two sets of flux measurements. At very low rate we will block one lepton beam and measure the flux of the other beam using the calorimeter at the target. Comparing the beam fluxes measured by the calorimeter for the two beams will tell us whether they are identical at the target (and by how much they differ if they are not identical). At a rate of 1 kHz (to minimize all dead times), we can acquire enough statistics on the beam distributions in under an hour. This will allow us to compare the beam fluxes to much better than 1%.

At the same time that we measure the flux using the calorimeter, we will measure part of the unused low-energy part of the beams in the dispersed region. By using both the dispersed detector and the calorimeter, we can cross-calibrate the two detectors. At normal rates, we cannot use the calorimeter so we will use the dispersed detectors to continuously monitor the two fluxes. This will tell us how the relative rates in the two beams scale when we increase the beam flux.

The electron and positron beams will be simultaneously incident on the same target. Thus, the CLAS proton acceptance will be the same for both reactions. Similarly, the proton momentum determination will be the same for both reactions.

We will trigger on two charged particles in opposite CLAS sectors. We will then use the $e^{\pm}$ angle and the proton kinematics to define the reaction (including determining the incident lepton energy), with only loose cuts on the $e^{\pm}$ momentum to identify elastic scattering reactions. (Note that the measurement of the angles of the outgoing leptons are determined primarily by the Region I drift chambers where there is no magnetic field. There should thus be little difference in the measurement of the electron and positron angles.) In this way, differences in the measurement of the electron and positron momentum vectors will have a minimal effect. Because the kinematics are overdetermined, there are several cross-checks that can be used to study this.

The largest source of experimental uncertainty is the different acceptance for electrons and for positrons. The first method of reducing these effects is to not trigger on a lepton (i.e.: to not require the Cerenkov counter or the electromagnetic calorimeter in the CLAS trigger). There are two remaining sources of acceptance differences: a) missing or inefficient detector channels and b) the CLAS geometry. The effects of missing or inefficient detector channels can be modeled using the CLAS monte carlo software package GSIM and the results of that modeling can be tested by comparing the results from the six different sectors of CLAS. This will reduce the effects of bad channels to significantly less than the statistical uncertainties.

Electrons and positrons have different geometrical acceptance in CLAS because one bends inward (toward the beamline) and the other bends outward. We will reduce this effect by operating the CLAS at the lowest possible magnetic field where we can still readily distinguish between elastic and inelastic scattering.

TABLE I: Anticipated systematic uncertainties. The error refers to the uncertainty in the e^+/e^- cross section ratio.

Source	Error (%)
e^+/e^- flux differences	0.2
Proton acceptance differences	0
e^+/e^- momentum measurement	0.1
e^+/e^- geometrical acceptance differences	< 1
e^+/e^- detector efficiency differences	0.1
inelastic contamination	0.1
Total	1

The remaining effects of the geometrical acceptances on the lepton acceptance can also be minimized. In general, there are two cases: a) large lepton scattering angle (small ε) and b) small lepton scattering angle (large ε). We will treat these separately.

For large lepton scattering angle, the CLAS acceptance is large and slowly varying (see Fig. 30). The azimuthal (ϕ) acceptance in each sector is significantly greater than 67% (ie: $\Delta\phi > 40^o$ out of a possible 60^o in each sector) for scattering angles $45^o < \theta < 130^o$. By making a tight cut on ϕ (e.g., $-20^o < \phi < 20^o$ in each sector), we can ensure that the electron and positron acceptances are identical. We also significantly reduce the affects of ϕ-focusing near the torus coils.

For small lepton scattering angles, the CLAS acceptance is small and rapidly varying. Therefore the electrons and positrons will have very different acceptances. We can compensate for this by reversing the CLAS torus field which, in effect, interchanges the scattered electron and positron trajectories. By averaging measurements with the two torus field polarities, we can completely account for the differences in the geometrical acceptance. However, we need to make sure when do this that the proton acceptances for the two torus field polarities are identical. Fortunately, when the leptons are at small angle, the proton will be detected at larger angles ($60^o < \theta_p < 90^o$) where the acceptance is larger and more slowly varying. By making a tight cut on ϕ_p (e.g., $-20^o < \phi_p < 20^o$ in each sector), we can ensure that the proton acceptances for the two field polarities are identical.

Differential $e^\pm$ attenuation in the several meter flight path from the target through the detectors will also be negligible, since $e^\pm$ at these energies is dominated by bremsstrahlung, which is identical for both particles.

There is a possibly significant target-related background from lepton virtual bremsstrahlung in the target resulting in $\gamma p \to p\pi^+\pi^-$ events where one of the pions is undetected. Most of these will be rejected by the same cuts that eliminate inelastic lepton scattering events $ep \to ep\pi^0$. The remaining background will merely dilute the e^+p/e^-p cross section ratio unless there is a charge anisotropy in the pion angular distribution (e.g., positively charged pions are more forward scattered than negatively charged pions). We can measure the contamination of the forward angle elastic leptons by using the CLAS EC, Cerenkov and LAC detectors to identify pions and leptons.

We will completely eliminate the background from $\gamma n \to p\pi^-$ by a) cutting the target to eliminate the target wall region and b) measuring the empty target and subtracting it from the full target runs.

In summary, the residual errors are likely to be the following (see Table I):

- an incorrect assignment of Q^2 and E_0 due to systematic errors in the measurement of the proton kinematic variables. This will cancel in the ratio e^+p/e^-p.
- the effect of detector channels changing characteristics. This will be reduced to less than the statistical error by a combination of simulation and comparison among the six sectors.
- the ratio of the incident lepton fluxes will be calculated and simulated, and directly measured as part of the experiment.
- the effects of differential electron and positron acceptances will be minimized with geometrical cuts and by reversing the CLAS torus field.

In conclusion, we believe that the systematic errors can be controlled to better than 1% because of the uniquely symmetric nature of the interaction under study, in combination with the large angle and momentum acceptance of CLAS.

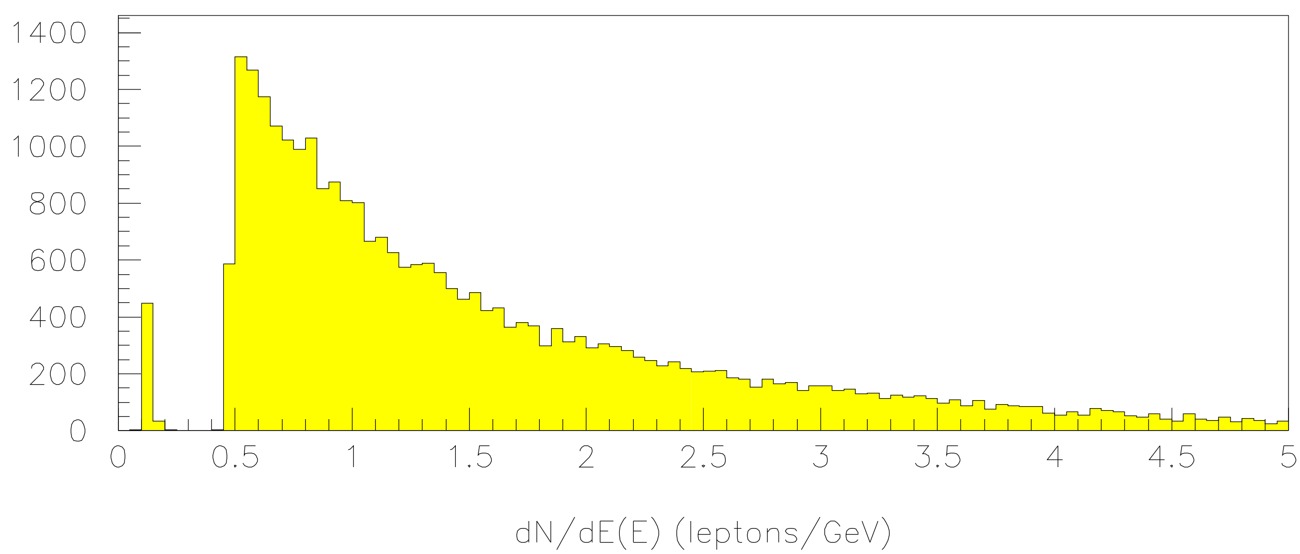

FIG. 29: The spectrum of lepton energies $\frac{d\mathcal{L}^{e^+e^-}}{dE}(E)$ incident on the cryotarget from a GEANT simulation. This yield corresponds to approximately 60 million electrons incident on the tagger radiator. The gap in energies seen in this figure is due to the low-energy collimators, which remove leptons that are too low in energy to contribute to the data of interest. The remaining very low energy leptons are a residual background.

H. Rate estimate

The 'beam' of positrons and electrons obtained from the apparatus has a wide range of energies. The rate estimate has been obtained by weighting the elastic scattering rate by the energy profile of the incident leptons and the CLAS acceptance. The lepton energy profile has

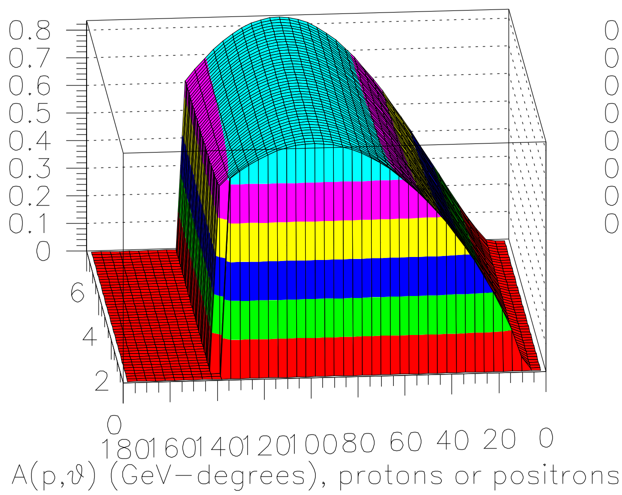

FIG. 30: Parameterized CLAS acceptances for single particles as a function of momentum and polar angle. This function takes into account the magnetic field value, the charge of the particle, and its momentum vector. Note that the acceptances are nearly identical for positrons and electrons over a broad kinematic range. This is an important feature of CLAS that helps to minimize systematic errors due to acceptance differences.

been calculated using a detailed GEANT simulation of the entire beamline apparatus, starting with a 5.7 GeV electron beam incident on the tagger radiator.

Elastic scattering is fully characterized by two kinematic variables. Because two-photon exchange is optimally revealed by its dependence on the variable ε, and because of the interest in extending the impact of these measurements to those at higher Q^2, a natural choice is to cast the problem in terms of these two variables.

In these variables, the double-differential counting rate is given by

$$\frac{d^2R}{dQ^2d\varepsilon} = \frac{d^2R}{dEd\Omega}\cdot\frac{dEd\Omega}{dQ^2d\varepsilon} = \frac{d}{dE}(\frac{dR}{d\Omega})\cdot\frac{dEd\Omega}{dQ^2d\varepsilon} \tag{6}$$

The rate per unit solid angle $\frac{dR}{d\Omega}$ is given by

$$\frac{dR}{d\Omega} = \int \frac{d\mathcal{L}^{e^+e^-}(E)}{dE}\cdot\frac{d\sigma}{d\Omega}dE \tag{7}$$

where $\frac{d\mathcal{L}^{e^+e^-}(E)}{dE}$ is the energy-dependent luminosity distribution of the leptons; this distribution, shown in Fig. 29, was derived from a GEANT simulation of the beamline. Substituting this expression for $\frac{dR}{d\Omega}$ into Eqn. 6 yields the final result:

$$\frac{d^2R}{dQ^2d\varepsilon} = \frac{d\mathcal{L}^{e^+e^-}(E)}{dE}\cdot\frac{d\sigma}{d\Omega}\cdot\frac{dEd\Omega}{dQ^2d\varepsilon} \tag{8}$$

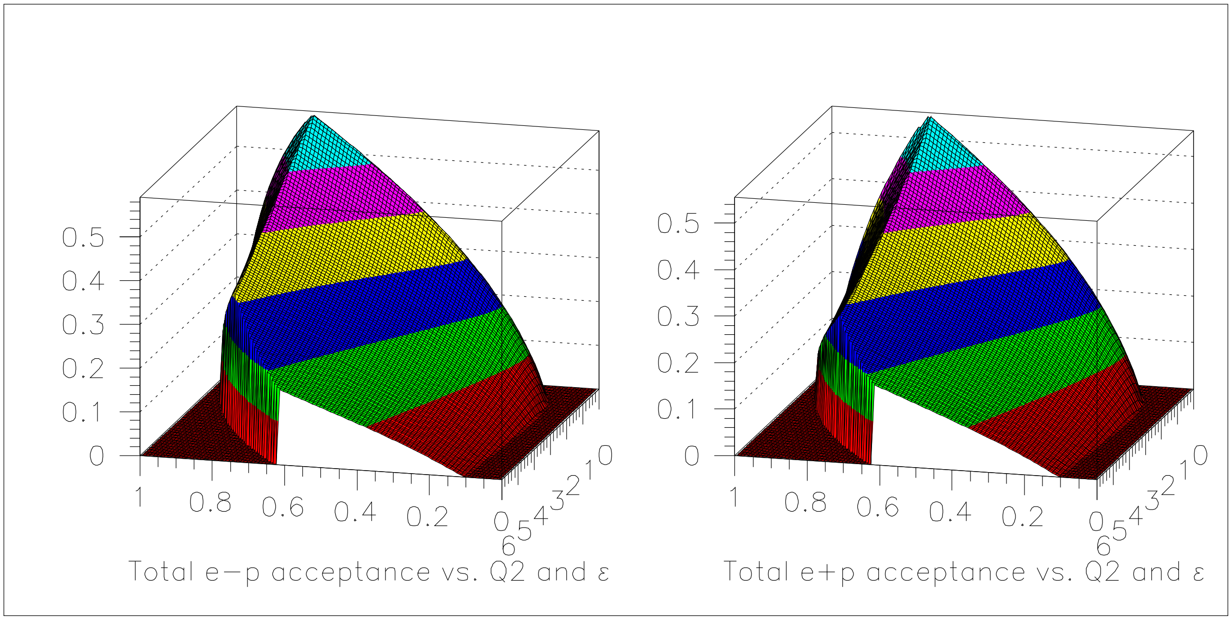

FIG. 31: Parameterized CLAS acceptances for elastic scattering events as a function of Q^2 and ε. Because the particles are completely correlated in this reaction, for each bin in $dQ^2 d\varepsilon$ the single particle acceptance (shown in Fig. 30 was computed for both particles and the smaller acceptance was taken as the event acceptance. No other losses were accounted for in the calculation, such as detection and reconstruction inefficiencies.

The rate calculation was performed numerically on a dense rectangular grid in Q^2 and ε to preserve accuracy; the final results were obtained by integrating these small bins into larger bins for data presentation. The number of counts N in a larger bin of $Q_1^2 < Q^2 < Q_2^2$ and $\varepsilon_1 < \varepsilon < \varepsilon_2$ is given by the time duration of the experiment multiplied by the rate $\frac{d^2R}{dQ^2 d\varepsilon}$ and integrated over the larger bin limits:

$$\int_{Q_1^2}^{Q_2^2} \int_{\varepsilon_1}^{\varepsilon_2} \frac{d^2N}{dQ^2 d\varepsilon} \cdot A(Q^2, \varepsilon)\ dQ^2 d\varepsilon \approx \sum_i \sum_j \frac{d^2N}{dQ^2 d\varepsilon} \cdot A(Q^2, \varepsilon)\ \Delta Q_i^2 \Delta\varepsilon_j \tag{9}$$

where $A(Q^2, \varepsilon)$ is the CLAS acceptance function shown in Fig. 31, which was derived from the single particle acceptance functions shown in Fig. 30. The RHS indicates the numerical integration procedure where i and j label the small bins in Q^2 and ε and $\frac{d^2N}{dQ^2 d\varepsilon}$ is an average value within the two-dimensional $Q^2 - \varepsilon$ bin. The distribution of total counts as a function of Q^2 and epsilon is shown in Fig. 32. Leptons of less than $25o$ in scattering angle were removed, since systematic errors in the acceptance ratio are not as well controlled for these angles.

The statistical quality of the data predicted by this rate calculation is indicated in Fig. 33 in one particular binning scheme. The Q^2 bins indicated are approximately the true bin centers, i.e. the Q^2 bins are asymmetric about the indicated values, and there are no gaps between the bins - all of the data is used. A band of $\pm 1\%$ is indicated on the figures for reference. The parameters used for the calculation are indicated in Table II.

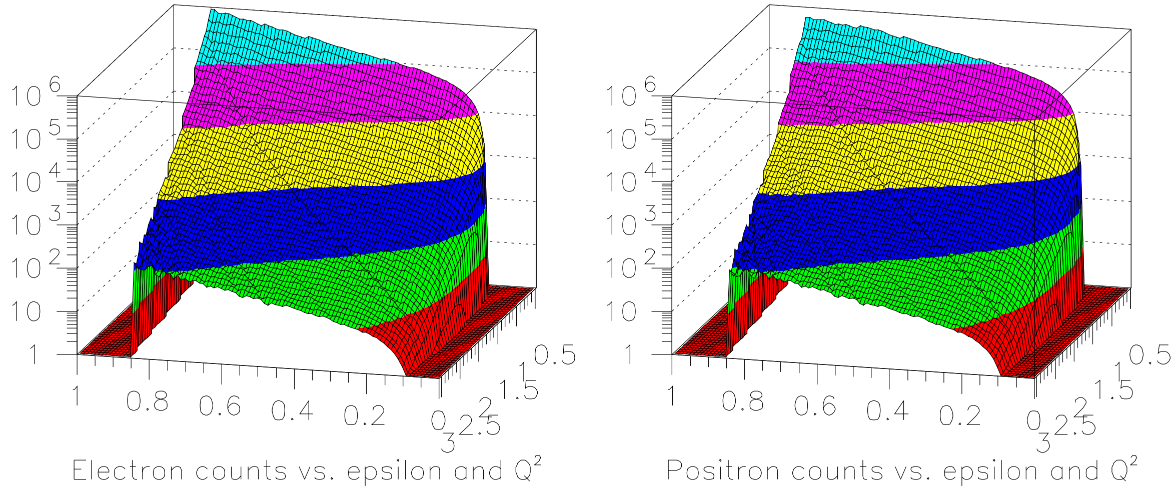

FIG. 32: The number of electron-proton and positron-proton scattering events as a function of Q^2 and ε from the rate calculation. Bins are 0.06 GeV^2 in Q^2 and 0.01 in ε.

TABLE II: Anticipated running conditions and beamtime request.

Item	Value
Primary electron beam energy	5.7 GeV
Primary electron beam current	1.0 μA
Radiator thickness	$5\%X_o$
Converter thickness	$2\%X_o$
Cryogenic hydrogen target length	20 cm
Torus current	1000 A
PAC days for data acquisition	27
Additional days for flux measurement and torus polarity changes	3
Additional days for commissioning of all devices	5
Total PAC days requested	**35**

IV. BEAM TIME REQUEST AND ANTICIPATED RESULTS

The running conditions and anticipated beam request are shown in Table II. The conditions selected are based on best known practices, GEANT simulation, and cryotarget technology that is known to be achievable. The limiting statistical error is for smallest epsilon. The total number of PAC days required is 35, which allows for 3 days of lepton flux measurements and several torus polarity changes, and 5 days for commissioning of the new devices (two flux detectors, magnet chicane, movable low-energy collimators, movable photon blocker, shielding configuration).

A plot of the expected data quality is shown in Fig. 33. This may be compared with the

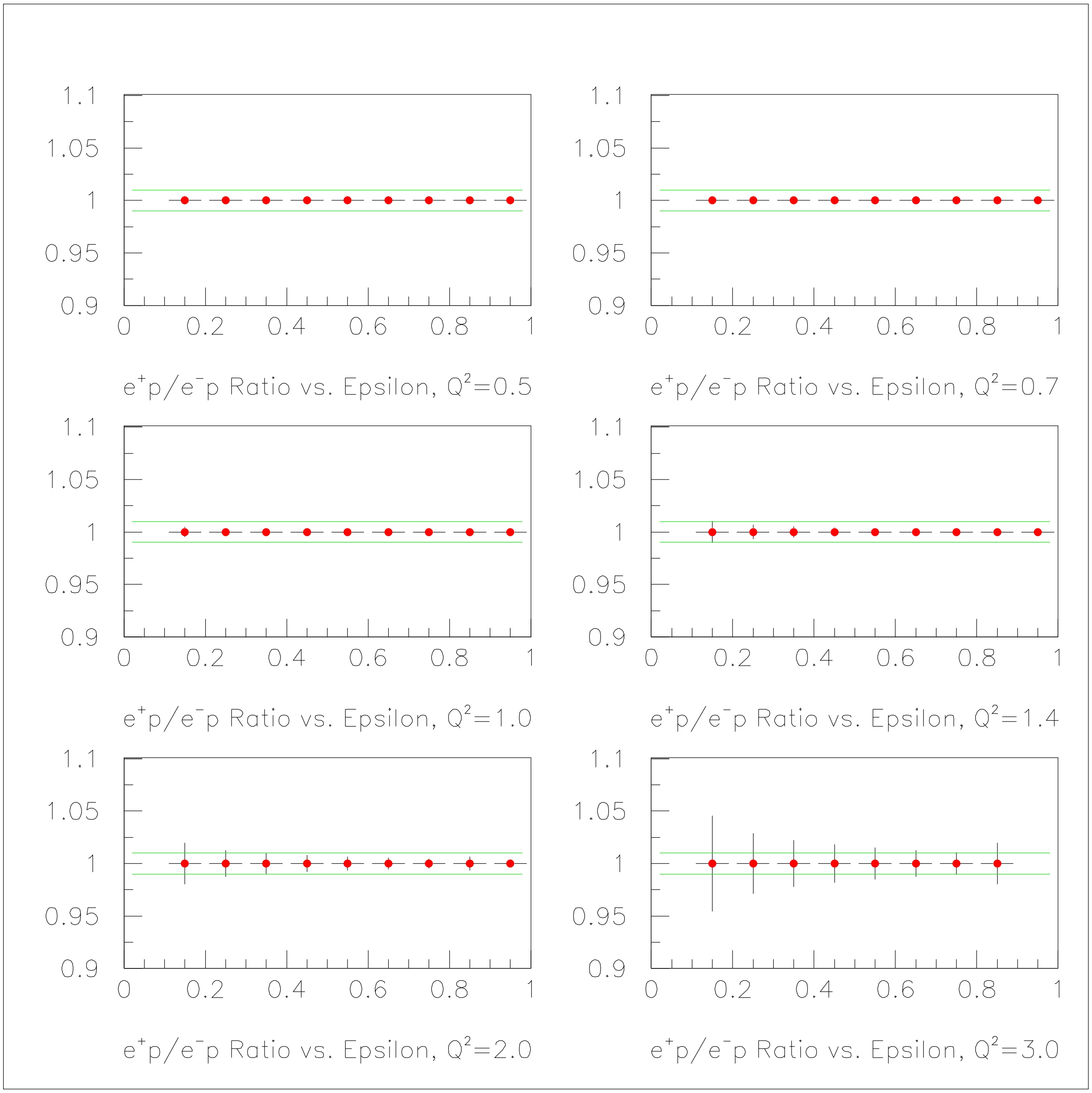

FIG. 33: Statistical errors in a particular binning scheme. The Q^2 values indicated in the captions are approximately true bin centers. A band of $\pm 1\%$ is indicated as a reference.

data of Fig. 3 which are shown on a much greater vertical axis range. A very significant improvement in our understanding of the epsilon dependence of this ratio would clearly be obtained from the CLAS data. This would in turn greatly strengthen our understanding of the role of the two-photon exchange in the elastic scattering process, and may resolve the currently dilemma concerning the discrepancy between the Rosenbluth-method analysis and the polarization analysis.

Figure 34 shows the projected results for the positron to electron ratio for several Q^2 bins. The size of the projected two-photon effects is based on the analysis described in Sec. II B 2. Figure 35 show the ε-dependence for each Q^2 bin, based on a linear fit to the points in Fig. 34 (including statistical and systematic uncertainties). The hollow blue square indicates the ε-

dependence of the TPE effect on the cross section as estimated from existing positron data [12].

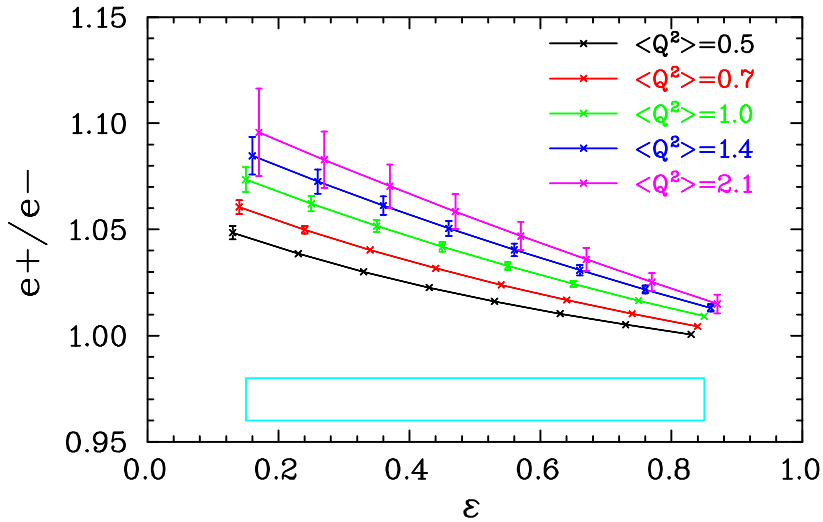

FIG. 34: Projected results and uncertainties for the positron-to-electron ratio. The error bars on the points are the statistical uncertainties. A $\pm 1\%$ systematic error band is shown at the bottom.

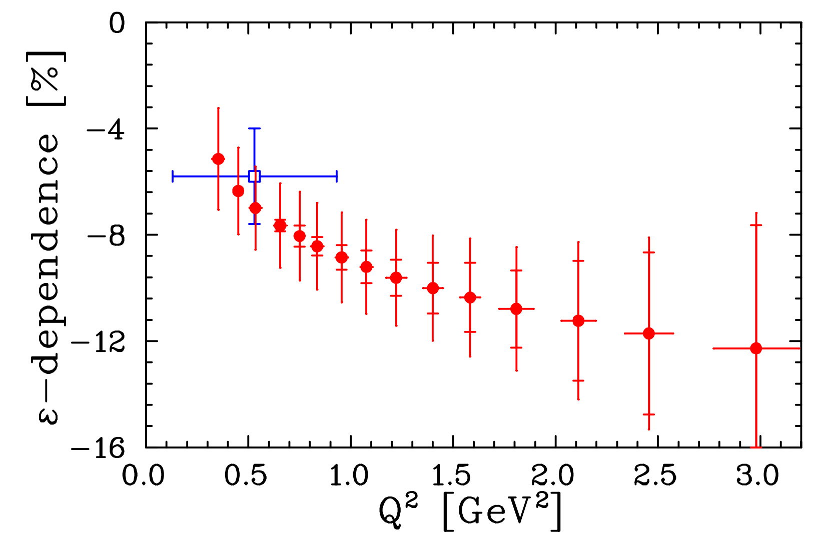

FIG. 35: Slope (ε-dependence) as a function of Q^2, based on a linear fit to the projected results. Inner error bars are based on the statistical uncertainty, outer error bars include the 1% systematic uncertainty. The blue square is the ε-dependence as determined from existing positron data.

V. EXPERIMENTS WITH SIMILAR PHYSICS GOALS

Experiment E04-019 was approved by PAC25 to measure the ε-dependence of polarization transfer measurements. This is sensitive to the ε-dependence of the two-photon amplitude $Y_{2\gamma}$ as defined in Ref. [6]. The discrepancy can be explained with small values of $Y_{2\gamma}$, well below the sensitivity of the experiment as proposed, but E04-019 will be able to determine if there is a large ε-dependence, or else set upper limits if no effect is observed. Because the experiment will determine the ε-dependence but not the *size* of $Y_{2\gamma}$, it will not by itself provide enough information to correct the polarization transfer results for two-photon effects. The positron measurements proposed here provide a *direct* determination of the two-photon contributions to the cross section, and thus the Rosenbluth extraction of the form factors, up to $Q^2 \approx 2.0$ GeV^2.

There were five proposals deferred by PAC25 that also examined TPE effects. One proposal was designed to check the polarization transfer results with a polarized target asymmetry measurement. If such a measurement were to agree with polarization transfer results, then it provides further support for the existence of the discrepancy and thus supports the case for the proposed experiment. If it were to disagree with the polarization transfer results, then it may be that the two-photon effects are not as large as currently believed. However, recent calculations and the re-examination of the existing positron data still support the idea that the two-photon are still larger than had been believed before the polarization transfer measurements, even if two-photon effects do not fully explain the form factor discrepancy. In this case, the proposed measurements are the most sensitive way to study these two-photon exchange effects.

PR04-020 was a proposal to study two-photon effect by making precise Rosenbluth measurements to check the linearity of the reduced cross section and to make precise measurements of the form factor ratio G_E/G_M. It was designed to look for non-linear terms coming from two-photon effects and to precisely measure the discrepancy to extract the size of the two-photon effects at large Q^2. The experiment is complementary to the proposed measurements here which will cleanly measure both the size and ε-dependence of the two-photon effects, but is limited to $Q^2 \approx 2$ GeV^2.

The three other proposals were designed to measure Born-forbidden polarization observables which provide direct access to two-photon exchange contributions. These observables are sensitive to the imaginary part of the two-photon exchange amplitudes, and so do not directly relate to the electron- and positron-proton cross sections, nor to the form factor measurements. However, they do provide entirely independent measurements of two-photon effects, and so are complementary to the measurements proposed here for testing models of TPE effects.

VI. CONCLUSIONS

There are indications that two-photon exchange corrections may be responsible for the discrepancy between Rosenbluth and polarization transfer measurements of the proton form factors. If so, then measurements of the discrepancy can be used to estimate the TPE contributions at large Q^2 [6, 24], as discussed briefly in Sec. II B 2. However, such an analysis is only useful if the discrepancy is fully explained by TPE corrections. Calculations of these effects are incomplete and existing positron measurements are limited to $Q^2 \approx 0.5$ GeV^2 and yield only a weak (three sigma) indication of a ε-dependence. Additional measurements are necessary to establish TPE corrections as the source of the discrepancy.

These proposed measurements of the ratio of electron- to positron-proton elastic scattering, will allow us to directly determine the TPE contribution to the cross section for $0.5 < Q^2 < 2$ GeV^2 and $0.1 < \varepsilon < 0.9$. In this region we will make a precise determination of the ε-dependence of the TPE contributions, which can be used to test models of the TPE corrections. At higher Q^2 values, $2 < Q^2 < 3$ GeV^2, we will measure the Q^2-dependence of the corrections, and determine the approximate ε-dependence. With this data, we can make a model-independent TPE correction to existing Rosenbluth extractions of G_E and G_M up to $Q^2 \approx 2-3$ GeV^2. This data will allow us to determine if two-photon exchange corrections fully explain the discrepancy between the values of G_E extracted by the Rosenbluth and polarization transfer measurements.

There are two possibilities:

1. We confirm that TPE are responsible for the observed difference between Rosenbluth and polarization transfer measurements. Our measurements will be used to constrain calculations of TPE. In addition, measurements of the Rosenbluth/polarization transfer discrepancy itself can then be used to extend these studies of the two-photon effects to larger Q^2.

2. We determine that the TPE corrections do *not* explain the form factor discrepancy. Then the explanation for the striking difference between Rosenbluth and polarization transfer measurements must be found elsewhere.

Either way, this proposed experiment will have very exciting results.

[1] L. Andivahis et al., Phys. Rev. D **50**, 5491 (1994).
[2] M. K. Jones et al., Phys. Rev. Lett. **84**, 1398 (2000).
[3] O. Gayou et al., Phys. Rev. Lett. **88**, 092301 (2002).
[4] J. Arrington, Phys. Rev. **C68**, 034325 (2003).
[5] M. E. Christy et al. (2004), nucl-ex/0401030.
[6] P. A. M. Guichon and M. Vanderhaeghen, Phys. Rev. Lett. **91**, 142303 (2003).
[7] J. Arrington, Phys. Rev. **C69**, 022201 (2004).
[8] P. E. Bosted, Phys. Rev. C **51**, 409 (1994).
[9] P. G. Blunden, W. Melnitchouk, and J. A. Tjon, Phys. Rev. Lett. **91**, 142304 (2003).
[10] A. Afanasev, S. Brodsky, and C. Carlson, presented at the DNP Meeting, Tuscon, AZ, Oct. 2003.
[11] Y. C. Chen, A. Afanasev, S. J. Brodsky, C. E. Carlson, and M. Vanderhaeghen (2004), hep-ph/0403058.
[12] J. Arrington, Phys. Rev. **C69**, 032201 (2004).
[13] M. N. Rosenbluth, Phys. Rev. **79**, 615 (1950).
[14] E. Offermann et al., Phys. Rev. C **44**, 1096 (1991).
[15] G. Fricke et al., Phys. Rev. C **45**, 80 (1992).
[16] N. Voegler et al., Phys. Rev. C **43**, 2172 (1991).
[17] P. Gueye et al., Phys. Rev. **C57**, 2107 (1998).
[18] Y. S. Tsai, Phys. Rev. **122**, 1898 (1961).
[19] L. W. Mo and Y.-S. Tsai, Rev. Mod. Phys. **41**, 205 (1969).
[20] L. C. Maximon and J. A. Tjon, Phys. Rev. **C62**, 054320 (2000), nucl-th/0002058.
[21] P. G. Blunden, W. Melnitchouk, and J. A. Tjon, in preparation.
[22] S. D. Drell and J. D. Sullivan, Phys. Lett. **19**, 516 (1965).
[23] J. Mar et al., Phys. Rev. Lett. **21**, 482 (1968).
[24] J. Arrington, in preparation.
[25] Y. S. Tsai, Tech. Rep., SLAC Report (1971).
[26] W. R. Nelson, T. M. Jenkins, R. McCall, and J. K. Cobb, Phys. Rev. **149**, 201 (1966).

[27] V. A. Batarin et al., Nucl. Instr. Methods **A 510**, 248 (2003).
[28] P. L. Mattern, IEEE Trans. Nucl. Sci. **NS-21**, 81 (1974).
[29] P. Degtyarenko, Proceedings of the Second Specialist's Meeting on Shielding Aspects of Accelerators, Targets and Irradiation Facilities **(SATIF2), 12-13 October 1995, CERN, Geneva, Switzerland**, 67 (1995).
[30] P. Degtyarenko, M. Kossov, and H.-P. Wellisch, Eur. Phys. J. **A 8**, 217 (2000).
[31] B. Mecking et al., Nucl. Instr. Methods **A 503/3**, 513 (2003).
[32] courtesy of Pavel Degtiarenko, author of GDINR
[33] See logs for runs 41708 and 41709.